DISCRETE AND CONTINUOUS
DYNAMICAL SYSTEMS
Volume **32**, Number **8**, August **2012**

doi:10.3934/dcds.2012.32.2879

pp. **2879–2912**

# BIFURCATIONS OF CANARD-INDUCED MIXED MODE OSCILLATIONS IN A PITUITARY LACTOTROPH MODEL

Theodore Vo

School of Mathematics and Statistics,
University of Sydney, Sydney, NSW, Australia

Richard Bertram and Martin Wechselberger

Department of Mathematics and Programs in Neuroscience and Molecular Biophysics,
Florida State University, Tallahassee, FL, USA

School of Mathematics and Statistics,
University of Sydney, Sydney, NSW, Australia

Abstract. Mixed mode oscillations (MMOs) are complex oscillatory waveforms that naturally occur in physiologically relevant dynamical processes. MMOs were studied in a model of electrical bursting in a pituitary lactotroph [34] where geometric singular perturbation theory and bifurcation analysis were combined to demonstrate that the MMOs arise from canard dynamics. In this work, we extend the analysis done in [34] and consider bifurcations of canard solutions under variations of key parameters. To do this, a global return map induced by the flow of the equations is constructed and a qualitative analysis given. The canard solutions act as separatrices in the return maps, organising the dynamics along the Poincaré section. We examine the bifurcations of the return maps and demonstrate that the map formulation allows for an explanation of the different MMO patterns observed in the lactotroph model.

1. **Introduction.** Nerve and endocrine cells exhibit complex oscillatory waveforms known as bursts [9]. These electrical patterns are characterized by periods of electrical spikes riding on top of an elevated voltage plateau, followed by periods of quiescence during which the cell is repolarized. We distinguish between two classes of bursting oscillations: plateau and pseudo-plateau bursting [21, 24, 28, 29, 32, 33]. Plateau bursting is characterized by periods of large amplitude fast spiking activity in the active (depolarized) phase whilst pseudo-plateau bursting is characterized by small amplitude spikes in the active phase. The bursting pattern is usually associated with higher levels of hormone or neurotransmitter secretion and there is evidence it may have important roles in neuronal signalling [22, 25]. In most bursting models in endocrine cells, the bursting oscillations are driven by the slow, systematic variation in the calcium concentration [21, 28, 32, 39]. However, in the pituitary lactotroph model that we consider [31], the pseudo-plateau bursting oscillations persist almost unaltered when the calcium concentration is fixed. This suggests an intrinsic bursting mechanism independent of the calcium.

2000 *Mathematics Subject Classification.* Primary: 34E17; Secondary: 92B25.

*Key words and phrases.* MMOs, bifurcations, geometric singular perturbation theory, canards, return maps.

RB is supported by NSF grant DMS 0917664.

| Parameter | Value | Definition |
|---|---|---|
| $C$ | $0-10$ pF | Membrane capacitance |
| $g_K$ | $0-10$ nS | Maximal conductance of delayed rectifier $K^+$ channels |
| $g_A$ | $0-25$ nS | Maximal conductance of A-type $K^+$ channels |
| $g_{Ca}$ | 2 nS | Maximal conductance of $Ca^{2+}$ channels |
| $V_{Ca}$ | 50 mV | Reversal potential for $Ca^{2+}$ |
| $V_m$ | $-20$ mV | Voltage value at midpoint of $m_\infty$ |
| $s_m$ | 12 mV | Slope parameter of $m_\infty$ |
| $V_K$ | $-75$ mV | Reversal potential for $K^+$ |
| $V_n$ | $-5$ mV | Voltage value at midpoint of $n_\infty$ |
| $s_n$ | 10 mV | Slope parameter of $n_\infty$ |
| $\tau_n$ | 40 ms | Time constant for $n$ |
| $V_a$ | $-20$ mV | Voltage value at midpoint of $a_\infty$ |
| $s_a$ | 10 mV | Slope parameter of $a_\infty$ |
| $V_e$ | $-60$ mV | Voltage value at midpoint of $e_\infty$ |
| $s_e$ | 10 mV | Slope parameter of $e_\infty$ |
| $g_L$ | 0.3 nS | Maximal conductance of leak current |
| $\tau_e$ | 20 ms | Time constant of $e$ |

TABLE 1. System parameters for the pituitary lactotroph model (1)

The model is a minimal description of the electrical activity in a pituitary lactotroph with the $Ca^{2+}$ concentration clamped [31]. The equations governing the evolution of the system are

$$\begin{aligned} C\frac{dV}{dt} &= -\left(I_{Ca}+I_K+I_A+I_L\right) \equiv g_{\max} f(V,n,e), \\ \frac{dn}{dt} &= \frac{n_\infty(V)-n}{\tau_n}, \\ \frac{de}{dt} &= \frac{e_\infty(V)-e}{\tau_e}, \end{aligned} \tag{1}$$

where $g_{\max} = 10$ nS is a typical conductance scale. The ionic currents are defined via Ohm's law by

$$\begin{aligned} I_{Ca} &= g_{Ca} m_\infty (V - V_{Ca}), \\ I_K &= g_K n (V - V_K), \\ I_A &= g_A a_\infty e (V - V_K), \\ I_L &= g_L (V - V_K), \end{aligned}$$

and the steady state activation functions have the form

$$x_\infty = \frac{1}{1+\exp\left(\frac{V_x - V}{s_x}\right)},$$

where $x$ represents an activation variable ($m, n$ and $a$). The steady state inactivation function is

$$e_\infty = \frac{1}{1+\exp\left(\frac{V - V_e}{s_e}\right)}.$$

Parameter values and definitions are listed in Table 1. The state variables $(V, n, e)$

represent the membrane potential and gating variables for the activation of $I_K$ and inactivation of $I_A$, respectively. The key parameters of interest are the membrane capacitance $C$, the conductance of delayed rectifier channels $g_K$ and the conductance of A-type channels $g_A$. Together, these parameters control the amplitude and number of spikes per burst [34].

By introducing a dimensionless time scale $t_s = t/k_t$ with reference time scale $k_t = \tau_e = 20\,\text{ms}$, system (1) transforms to

$$\begin{aligned} \frac{C}{g_{\max}k_t}\frac{dV}{dt_s} \equiv \varepsilon\frac{dV}{dt_s} &= f(V,n,e), \\ \frac{dn}{dt_s} &= \frac{k_t}{\tau_n}(n_\infty(V)-n) \equiv g_1(V,n), \\ \frac{de}{dt_s} &= \frac{k_t}{\tau_e}(e_\infty(V)-e) \equiv g_2(V,e), \end{aligned} \tag{2}$$

and we are able to identify the typical time scales of the lactotroph model [34].[1] The membrane potential $V$ evolves on a fast timescale (given to leading order by $C/g_{\max} < 1$ ms) whilst $(n,e)$ evolve on slow timescales ($\tau_e = 20\,\text{ms}$ and $\tau_n = 40$ ms). In particular, decreasing $C$ increases the timescale separation which is reflected in the singular perturbation parameter $\varepsilon = \frac{C}{k_t g_{\max}} \ll 1$. Thus, system (2) is a singularly perturbed problem with slow variables $(n,e)$ and fast variable $V$ and perturbation parameter $\varepsilon$ evolving on the slow (dimensionless) timescale $t_s$.

Switching to a dimensionless fast timescale $t_f = t_s/\varepsilon$ yields an equivalent representation of (2):

$$\begin{aligned} \frac{dV}{dt_f} &= f(V,n,e), \\ \frac{dn}{dt_f} &= \varepsilon g_1(V,n), \\ \frac{de}{dt_f} &= \varepsilon g_2(V,e). \end{aligned} \tag{3}$$

Using geometric singular perturbation theory [10, 17], one of the key results shown in [34] is that the pseudo-plateau bursting is actually a canard-induced mixed-mode oscillation (MMO) [2] where a MMO pattern corresponds to a switching between small amplitude oscillations (spikes) and large amplitude relaxation type excursions (Figure 1). The basic classification of MMOs is based on the number of small oscillations $s$ and the number of large oscillations $L$, typically denoted $L^s$ and called the MMO signature. The MMOs are the result of the interaction between local and global mechanisms. The small amplitude oscillations are caused by a local twisting of trajectories near a folded singularity [26, 35, 38]. The large spikes arise from the global return of trajectories. For an extensive survey of canard induced MMOs, we refer to [6].

A primary goal of this study is to understand the dynamics of spike adding in pseudo-plateau bursting. That is, to understand why the spike number in a burst increases or decreases as one of two key parameters (maximal conductances of two ionic currents) is varied. Such studies have been performed previously on plateau

[1] In general, one also has to define a typical voltage scale $k_v$ and define the dimensionless voltage $v = V/k_v$ to obtain a dimensionless system and, hence, the typical time scales of the system (see [34] for details). Here, $k_v$ does not influence the order of the time scales and we keep the original voltage variable $V$ for easier comparison with data.

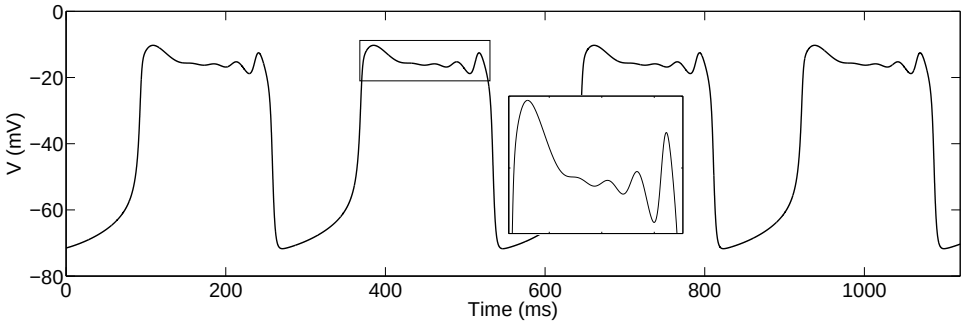


FIGURE 1. $1^4$ MMO pattern observed in (1) for $C = 2$ pF, $g_K = 4.1$ nS and $g_A = 4$ nS.

bursting [30] and, more recently, on pseudo-plateau bursting [24, 33]. In Section 2 we provide a detailed investigation of the bifurcation structure of pseudo-plateau bursting (MMOs) similar to [24] to determine the regions in parameter space where spike transitions occur. Following the work done in [36, 37] for a stellate cell model, we focus primarily on $1^s$ and related MMO patterns. In Section 3 we give a summary of the geometric analysis presented in [34] where the 3D system (1) is formally decomposed into a 2D slow subsystem coupled to a 1D fast subsystem. This slow/fast analysis helps us to understand the pattern of spike additions and the dynamics underlying them. We also review the pertinent canard theory [2, 26, 35, 38] and examine the geometry of the system for $C \neq 0$ in detail. In particular, we calculate the intersections of invariant manifolds [3, 4, 5] to identify the exact locations of canards which are boundaries of different MMO patterns. The comparison of the singular limit predictions with the observed MMO boundaries shows that the singular limit analysis is able to predict these different MMO boundaries sufficiently well.

In Section 4, we introduce a suitable 1D Poincaré (first return) map [13, 15, 19, 23, 36, 37] which covers the essential dynamics, as an alternative method for understanding the spike adding transitions. In Section 5 we investigate the bifurcations of the return maps which explain the bifurcation structure of MMOs observed in Section 2. Again, certain topological features of the return maps can be predicted from the corresponding singular limit return maps and, hence, explain certain bifurcation structures. Thus, the bifurcation analysis of system (1) provides a view of the sequence of spike-adding transitions and the associated periodic bursting solutions, while the slow/fast analysis and 1D return maps help us to understand why the spike-adding transitions occur. Finally, we conclude with a discussion in Section 6.

## 2. Bifurcations of MMOs.

In [34], the authors identified the region in $(g_K, g_A)$ parameter space where MMOs exist for $C = 2$ pF. A discussion of the boundaries delimiting the bursting regime was provided and an argument given for how the MMOs change in the interior of the bursting region. Here, we extend that work and perform a full system bifurcation analysis of (1) with particular emphasis on identifying a common sequence of bifurcations from a stable $1^s$ MMO pattern to a stable $1^{s+1}$ MMO pattern, $s \geq 0$.

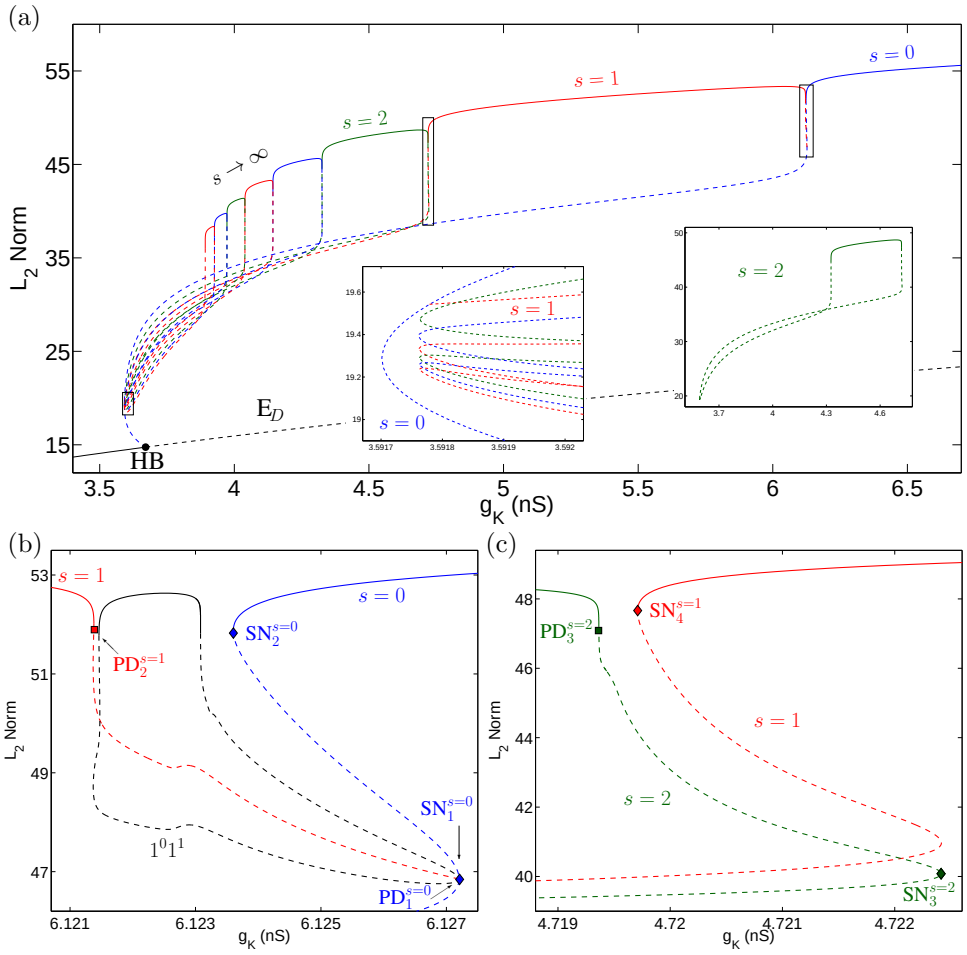


FIGURE 2. Bifurcations of system (1) along the horizontal line $g_A = 4$ nS for $C = 2$ pF. (a) The left inset shows a neighbourhood of the saddle-node of periodics of the bursting families for $s \geq 2$. Only the branch $s = 1$ connects to the Hopf branch at a PD bifurcation point. The right inset shows that the $s = 2$ bursting family is a closed isola of periodic orbits. This is true for all bursting families $s \geq 2$. (b) Region between the spiking ($s = 0$) and first bursting ($s = 1$) families where an isola of orbits with signature $1^01^1$ have been computed. Note that the $s = 1$ branch connects to the $s = 0$ branch at a PD bifurcation point. (c) Transition region between $s = 1$ and $s = 2$ MMOs.

2.1. **Horizontal bifurcations.** By fixing $C = 2$ pF, $g_A = 4$ nS, we consider only those bifurcations that arise from variations in $g_K$, the biophysical parameter that controls the repolarizing current $I_K$. Using AUTO [7, 8], a bifurcation diagram was calculated as shown in Figure 2, where $g_K$ is the principal continuation parameter and $L_2$ norm refers to the standard Euclidean norm (for equilibrium points) or the $L_2$ norm (for periodic solutions).

The spiking family (labelled $s = 0$ in Figure 2) connects to the depolarized equilibrium curve [2] (black $E_D$) at subcritical Hopf bifurcations (HB) at $g_K \approx 3.67$ nS and $g_K \approx 36.99$ nS (only one Hopf bifurcation is shown). The first bursting family (labelled $s = 1$) connects to the spiking family at period doubling (PD) points at $g_K \approx 6.127$ nS and $g_K \approx 3.592$ nS. The rest of the MMO families are isolated closed curves of periodic orbits. These isolas are born in saddle-node of periodic orbits bifurcations in a neighbourhood of $g_K \approx 3.592$ nS and possess stable plateau regions which never overlap. Between each pair of MMO families $s = n$ and $s = n + 1$ for $n = 0, 1, 2, \ldots$, there is a small interval where neither branch is stable. In these $g_K$ intervals, we find isolas of more complicated MMO patterns. The MMO signature in these parameter intervals is always some mixture of $1^n$ and $1^{n+1}$. Figure 2(b) shows only one of these isolas with signature $1^0 1^1$. The stability plateau of the MMOs in these parameter intervals decreases rapidly with the complexity of the MMO signature.

Figure 2(b) shows the $g_K$ window where the $s = 0$ spiking and $s = 1$ bursting curves meet along with the $1^0 1^1$ MMO. In order of decreasing $g_K$, there are 4 significant bifurcations for the $s = 0$ spiking and $s = 1$ MMOs. The saddle-node of periodic orbits (SN) point on the spiking branch at $g_K \approx 6.127$ nS labelled $\mathrm{SN}_1^{s=0}$ marks the location where the first bursting family and additional isolas of mixed MMO type are born. There is also a period doubling (PD) bifurcation labelled $\mathrm{PD}_1^{s=0}$ at almost the same $g_K$ value. The spiking branch $s = 0$ remains stable until the SN point marked by $\mathrm{SN}_2^{s=0}$ at $g_K \approx 6.1235$ nS is reached. Then there is a PD point labelled $\mathrm{PD}_2^{s=1}$ at $g_K \approx 6.1213$ nS where the $s = 1$ bursting branch becomes stable. The parameter window between $\mathrm{PD}_2^{s=1}$ and $\mathrm{SN}_2^{s=0}$ is filled with stable branches of isolas with mixed MMO signature (only branch shown is $1^0 1^1$).

The transition from the $s = 1$ bursting branch to the $s = 2$ bursting branch differs slightly from the spiking to bursting transition as the $s = 1$ and $s = 2$ families do not connect to each other (Figure 2(c)). Nevertheless, the bifurcation sequence is similar. The $1^2$ isola is born as an unstable family of orbits for decreasing $g_K$ in a SN point (labelled $\mathrm{SN}_3^{s=2}$) whilst the $1^1$ branch remains stable. The $s = 1$ branch then loses stability at the SN point indicated by $\mathrm{SN}_4^{s=1}$ and another parameter window of complex isolas is encountered where the stable MMOs have signatures which are mixtures of $1^1$ and $1^2$. As $g_K$ decreases further, the $s = 2$ branch becomes stable in a PD point corresponding to the label $\mathrm{PD}_3^{s=2}$.

There are additional bifurcations of the $s = 1$ and $s = 2$ curves that have been omitted from the discussion as they have little bearing on later results. For the remaining transitions between MMO families, the sequence of bifurcations is the same. Thus it is sufficient to consider only the transition from spiking to bursting and from $s = 1$ to $s = 2$ to understand the bifurcation structure of the MMOs away from the saddle-node of periodic orbits region (near $g_K \approx 3.59$ nS; inset Figure 2(a)).

2.2. **Vertical bifurcations.** By fixing $g_K = 4.1$ nS, we consider only bifurcations that arise due to variations in $g_A$, the biophysical parameter that controls the sub-threshold current $I_A$. The resulting bifurcation diagrams for $C = 2$ pF and $C = 0.1$ pF are shown in Figures 3 and 4, respectively. As before, we consider (and label) only those bifurcations which are crucial to our discussion.

[2]The equilibrium is a depolarized steady state for small $g_K$. After the first Hopf it becomes a saddle and after the second Hopf it becomes a hyperpolarized steady state.

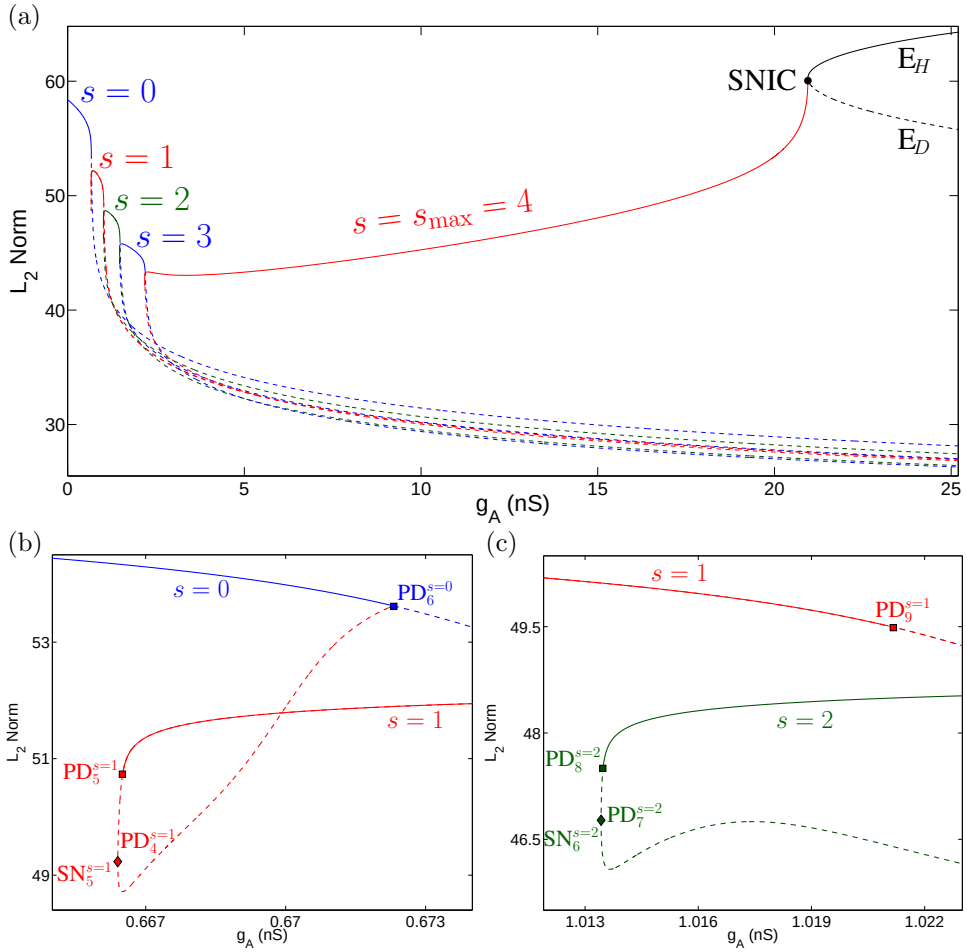


FIGURE 3. (a) Bifurcations of MMOs along the vertical line $g_K = 4.1$ nS for $C = 2$ pF where $s_{\max} = 4$. (b) Blown-up view of the transition from spiking to bursting. (c) Transition region between $s = 1$ and $s = 2$ MMOs: we observe regions of bistability.

For $C = 2$ pF, the $s = 1$ bursting family connects to the spiking branch at a PD point and the remaining MMO branches are disconnected. Unlike the horizontal case, there are no parameter windows in which more complex MMO patterns can be found (Figure 3(b) and (c)). Instead, there are regions in which the stable plateau of neighbouring MMO branches may overlap and the system exhibits bistability between two different bursting states. These bistable parameter windows are $C$ dependent. As $C$ decreases, the widths of the intervals of the bistable regions decreases. For sufficiently small $C$, the stable branches no longer overlap (Figure 4 inset shows this for $C = 0.1$ pF) and parameter windows with more complex MMO patterns can be found (not shown). All bursting families terminate in homoclinic orbits (not shown) for $g_A$ values well outside the physiologically meaningful domain ($g_A > 500$ nS).

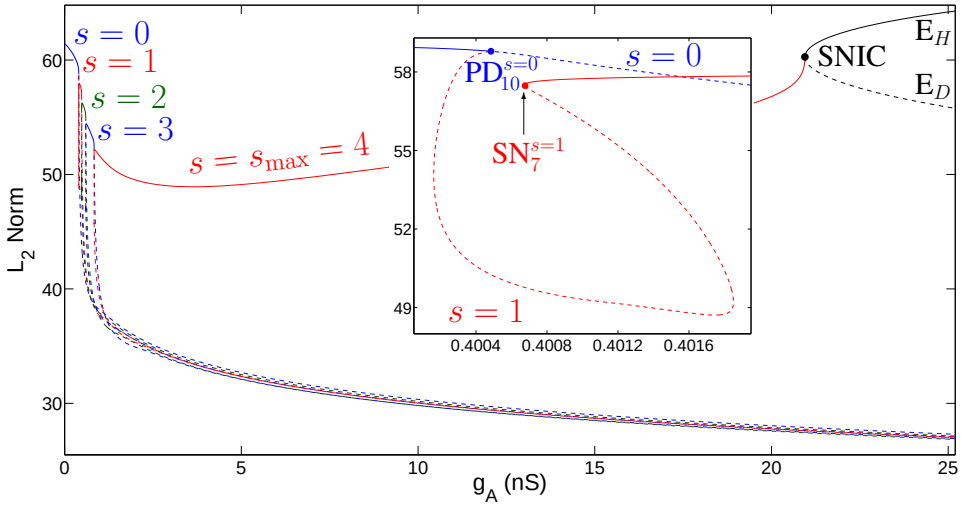


FIGURE 4. Bifurcations of MMOs along the vertical line $g_K = 4.1$ nS for $C = 0.1$ pF where $s_{\max} = 4$: The inset shows that there is no overlap between the stable portions of the MMO branches (compare with Figure 3).

For $C = 2$ pF, the sequence of bifurcations in the transition from spiking to bursting MMOs (in the direction of increasing $g_A$) is commenced by the $SN_5^{s=1}$ point where the $1^1$ orbit is created (Figure 3(b)). The stable upper branch immediately loses stability in a PD bifurcation $PD_4^{s=1}$ at virtually the same $g_A$ value. The $s = 1$ MMO curve becomes again stable at another PD point $PD_5^{s=1}$ whilst the spiking branch also remains stable. This bistability endures until a PD point $PD_6^{s=0}$ is reached on the $s = 0$ branch where the $1^1$ family connects with the $1^0$ family. Beyond this point, the $1^1$ family is stable and the $1^0$ branch is unstable.

For the change from $s = 1$ to $s = 2$ for $C = 2$ pF, the $s = 2$ family is born in the $SN_6^{s=2}$ point with a stable upper branch and an unstable lower branch. The stable upper branch rapidly loses stability at a PD point $PD_7^{s=2}$ in Figure 3(c) (so that both the SN and PD points virtually coincide). The upper branch of the $s = 2$ curve eventually regains stability at another PD point $PD_8^{s=2}$. There is a small bistable window before the $s = 1$ MMO becomes unstable in a PD bifurcation $PD_9^{s=1}$. Subsequently, the $s = 1$ MMO remains unstable and the $s = 2$ MMO remains stable until the next MMO transition. In general, the sequence of bifurcations between MMO families $s = n$ and $s = n+1$ ($n = 1, \ldots, s_{\max} - 2$, where $s_{\max}$ denotes the maximum number of small oscillations observed) follows a similar pattern to the $s = 0$ to $s = 1$ transition. In our case, we have $s_{max} = 4$ and the above description of bifurcation sequences also covers the transiti on from the $s = 2$ to the $s = 3$ branch.

The last transition from the $s_{\max} - 1$ branch to the $s_{\max}$ branch requires special attention. The $s_{\max}$ branch is born in a SN point in the usual way, but the upper branch is born stable and remains so. Bistability between $s_{\max} - 1$ and $s_{\max}$ exists until the $s_{\max} - 1$ family loses stability via a PD bifurcation. The $s_{\max}$ branch

remains stable until it terminates in a saddle-node on invariant circle (SNIC) bifurcation (Figures 3 and 4), after which the attractor of the system is a hyperpolarized state (labelled $\mathrm{E}_H$ in Figures 3 and 4).

2.3. **The MMO regime.** In light of Sections 2.1 and 2.2, Figure 5(a) shows a refined version of the $C = 2$ pF $(g_K, g_A)$-parameter bifurcation diagram from [34]. We also include a refinement of the $C = 0$ pF $(g_K, g_A)$-parameter bifurcation diagram (Figure 5(b)) from [34] (for easier comparison between the $C = 2$ pF and $C = 0$ pF figures), but defer the discussion to Section 3.

For the $C = 2$ pF diagram in Figure 5(a), we calculated the bursting boundaries using numerical continuation [7, 20]. The rightmost boundary of the bursting region, which follows $\mathrm{SN}_2^{s=0}$ (Figure 2(b)), is a curve of SN points and marks the location where the spiking family loses stability. Note that a $(g_K, g_A)$-continuation of the point $\mathrm{SN}_1^{s=0}$ generates a similar curve to the right of $\mathrm{SN}_2^{s=0}$ (not shown). In fact, the $\mathrm{SN}_1^{s=0}$ and $\mathrm{SN}_2^{s=0}$ curves coalesce at a limit point near the corner of the bursting regime. The left and lower boundaries of the bursting regime form a single curve of PD points. These arise from a 2-parameter continuation of the $\mathrm{PD}_6^{s=0}$ point (Figure 3(b)). The $\mathrm{PD}_6^{s=0}$ point also generates a nearly vertical right border (not shown) which sits virtually on top of the $\mathrm{SN}_1^{s=0}$ border (compare with Figure 2(b)). Moreover, the right boundary generated by $\mathrm{PD}_6^{s=0}$ passes through the curve of SN points. To clarify, in Figure 5(a) we depict the right and lower boundaries of the MMO region as the $\mathrm{SN}_2^{s=0}$ branch and the $\mathrm{PD}_6^{s=0}$ branch up to its intersection with the $\mathrm{SN}_2^{s=0}$ branch.

There is a very thin strip in the $s_{\max} = 1$ sector where the MMO signature is some combination of $1^0$ and $1^1$. This thin strip is delimited on the right by the $\mathrm{SN}_2^{s=0}$ branch and on the left by a PD branch obtained from continuation of $\mathrm{PD}_2^{s=1}$ (not shown). For $g_A$ away from the lower PD border, the $\mathrm{PD}_2^{s=1}$ branch sits to the left of the $\mathrm{SN}_2^{s=0}$ branch (hence the complex MMO region). For smaller $g_A$, the situation is reversed and the $\mathrm{PD}_2^{s=1}$ branch sits to the right of the $\mathrm{SN}_2^{s=0}$ branch thus indicating bistable MMO regions (see Figure 3(b)).

As shown in Section 2.1, a $1^n$ MMO loses stability at a SN point whilst the adjacent $1^{n+1}$ MMO becomes stable shortly after at a PD point. Two parameter continuation of these PD points generates a first approximation to the boundaries between MMO regimes. For instance, continuation of the $\mathrm{PD}_3^{s=2}$ point (Figure 2(c)) gives the border between $s_{\max} = 1$ and $s_{\max} = 2$. Continuation of the $\mathrm{SN}_4^{s=1}$ point (not shown) would of course generate a boundary very close to (and to the right of) the $\mathrm{PD}_3^{s=2}$ border. We could then use this to identify the thin wedges in parameter space where the complex MMO patterns appear. Similarly, continuation of the PD points in Figure 3 where the $s = n$ branch loses stability and the $s = n + 1$ branch gains stability generate thin strips in $(g_K, g_A)$ space where bistability holds. In either case (complex MMOs or bistability), the strip covered in the $(g_K, g_A)$ plane is extremely thin. As such we concern ourselves mainly with the boundaries where a spike is added to the MMO pattern.

From the bifurcation analysis we have identified the regions in parameter space where the spike transitions occur in the pseudo-plateau bursting. We turn our attention now to the question of what underlying mechanisms cause these transitions. We use geometric singular perturbation theory as the basis of our understanding.

3. **Geometric singular perturbation analysis of MMOs.** Here we review the geometric singular perturbation analysis of system (1) [34] and the appropriate

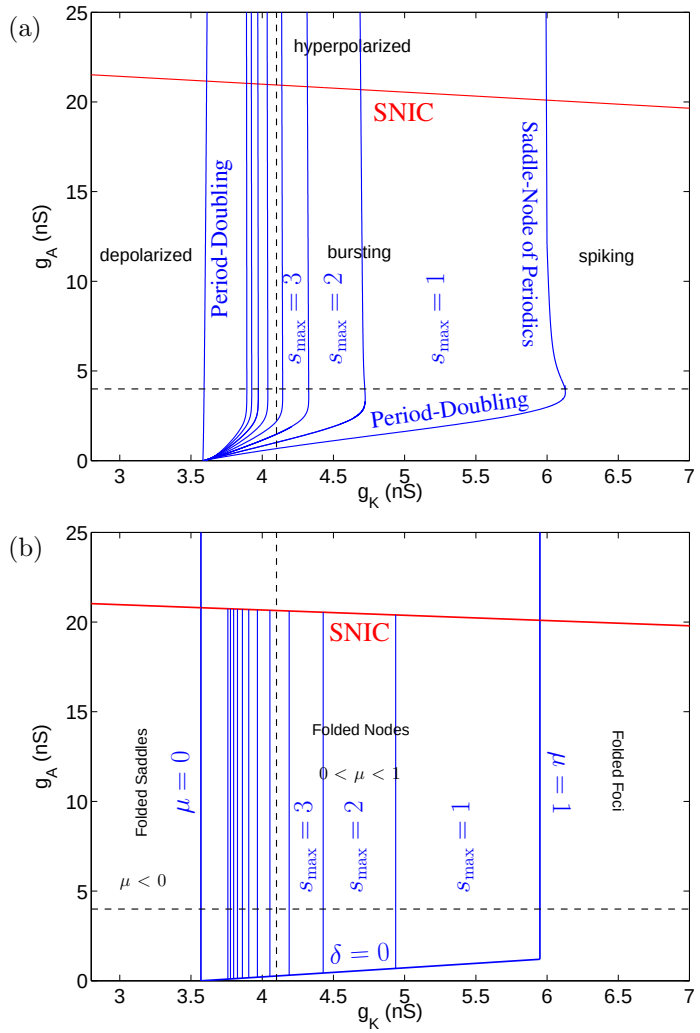


FIGURE 5. Boundaries of MMO patterns in $(g_K, g_A)$ parameter space: (a) observed in the full 3D system (1) and (b) predicted from the singular limit (see Section 3.2). Vertical lines in (b) between $\mu = 0$ and $\mu = 1$ indicate candidate boundaries for the rotational sectors in the fully perturbed problem (1) corresponding to odd integer values of $\mu^{-1}$. Horizontal dashed lines correspond to $g_A = 4$ nS (see Figure 2). Vertical dashed lines correspond to $g_K = 4.1$ nS (see Figure 3).

canard theory [2, 26, 35, 38]. Dynamically, the lactotroph model can be partitioned into slow and fast subsystems by taking the singular limit $C \to 0$ ($\varepsilon \to 0$) on the slow and fast timescales, respectively. The 2D slow limiting system, $C \to 0$ ($\varepsilon \to 0$)

in system (2),

$$\begin{aligned} 0 =& f(V,n,e),\\ \frac{dn}{dt_s} =& g_1(V,n),\\ \frac{de}{dt_s} =& g_2(V,e), \end{aligned} \tag{4}$$

is called the reduced system and the 1D fast limiting system, $C \to 0$ ($\varepsilon \to 0$) in system (3),

$$\begin{aligned} \frac{dV}{dt_f} =& f(V,n,e),\\ \frac{dn}{dt_f} =& 0,\\ \frac{de}{dt_f} =& 0, \end{aligned} \tag{5}$$

is called the layer problem. Geometric singular perturbation theory [2, 10, 17, 27] pieces together the information obtained from the lower dimensional subproblems (4), (5) to provide a unified global description of the lactotroph model (1), as we will explain in the following.

3.1. **The reduced and layer problems.** The set of critical points of the layer problem (5) is called the critical manifold, defined by

$$S := \left\{(V,n,e) \in \mathbb{R}^3 : f(V,n,e) = 0\right\}. \tag{6}$$

It was shown in [34] that this manifold of equilibria is a folded surface with respect to the fast variable $V$ as shown, e.g., in Figures 6 and 7. This follows directly from the stability analysis of the two-dimensional set of equilibria in (5) which possesses a subset of equilibria with a zero eigenvalue. In the physiological range of $(n,e)$ this subset consists of two disjoint sets, the one-dimensional fold curves

$$L^{\pm} := \{(V,n,e) \in S : f_V(V,n,e) = 0\} \tag{7}$$

which divide $S$ into attracting ($S_a^{\pm}$) and repelling ($S_r$) sheets. There also exists parameter sets of $(g_K, g_A)$ where the two fold curves $L^{\pm}$ join in the physiological domain. In this case, the critical manifold forms a cusp (not shown here; see [34]).

The critical manifold $S$ is not only the manifold of equilibria for the layer problem (5) but it also represents the phase space of the reduced problem (4) which is a differential algebraic system describing the evolution of the slow variables $(n,e)$ constrained to $S$. Since $n$ (and $e$) enter $f(V,n,e)$ linearly, $S$ has, e.g., a graph representation $n = n(V,e)$. As a result, a complete description of the reduced problem (4) is obtained by projecting onto the single base $(V,e)$ of $S$. The resulting equations are

$$\begin{aligned} -f_V \frac{dV}{dt_s} =& f_n g_1 + f_e g_2,\\ \frac{de}{dt_s} =& g_2, \end{aligned} \tag{8}$$

where $n = n(V,e)$ satisfies (6). System (8) is singular at the fold curves $L^{\pm}$. The finite time blow-up of the system at the folds can be removed by rescaling time

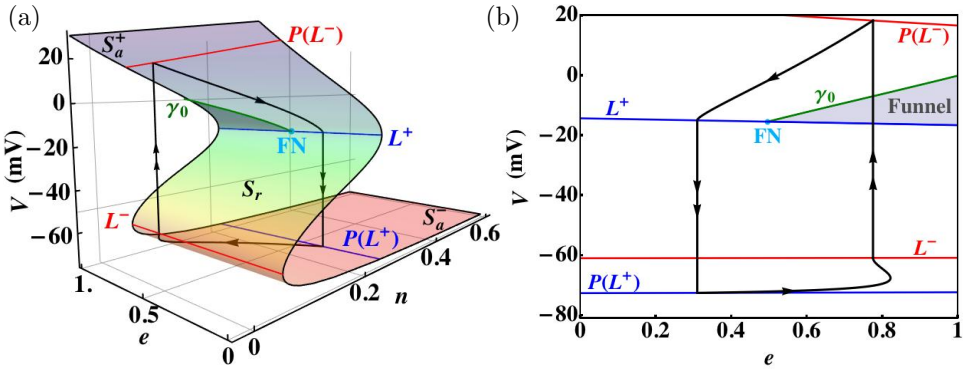


FIGURE 6. Critical manifold $S$ and singular relaxation orbit for $g_K = 4.1$ nS, $g_A = 0.2$ nS: (a) 3D view and (b) projection onto $(e, V)$-space. The fast jumps (double arrow) join with the slow segments (single arrow) on the attracting sheets $S_a^{\pm}$. The fold curves $L^{\pm}$ and their projections $P(L^{\pm})$ indicate where the reduced flow jumps and where it lands, respectively. The grey shaded region between $L^+$ and the strong canard (green, $\gamma_0$) is the funnel of the folded node (FN).

$(t_s = -f_V t_d)$ to give the desingularized system

$$\begin{aligned} \frac{dV}{dt_d} &= f_n g_1 + f_e g_2 \equiv F, \\ \frac{de}{dt_d} &= -f_V g_2, \end{aligned} \tag{9}$$

the flow of which is equivalent to (8) on the attracting sheets $S_a^{\pm}$ but is reversed on the repelling sheet $S_r$ due to the rescaling of time. Thus the reduced flow (8) can be understood by analysing the desingularized system (9).

The desingularized system (9) possesses, in general, two types of equilibria: *ordinary* ($g_1 = 0, g_2 = 0$) and *folded* ($F = 0, f_V = 0$). Ordinary singularities are equilibria of the desingularized flow (9), of the reduced flow (8) and of the original system (1). Folded singularities on the other hand are generally not equilibria of (8) or (1). They are classified as equilibria of (9) and can generate counter-intuitive behaviour, essentially due to the cancellation of a simple zero in (8) [26]. More specifically, they enable solutions of the reduced flow (8) to cross the fold curve in finite time with non-zero speed from $S_a$ (through the folded singularity) to $S_r$ (except folded foci).

A *folded node singularity* is especially important to the bursting model (1) and occurs in generic slow-fast systems with two (or more) slow variables [26, 35, 38]. Folded nodes allow for an entire sector of trajectories to pass from the upper attracting branch $S_a^+$ of the critical manifold to the repelling branch $S_r$, and to follow that repelling branch for an $\mathcal{O}(1)$ time on the slow timescale. Such solutions are called *singular canards*. The sector of canard solutions (the singular funnel) is bounded by the fold curve $L^+$ and by the *strong canard* $\gamma_0$, which is the unique trajectory tangential to the strong eigendirection of the folded node (see Figures 6 and 7).

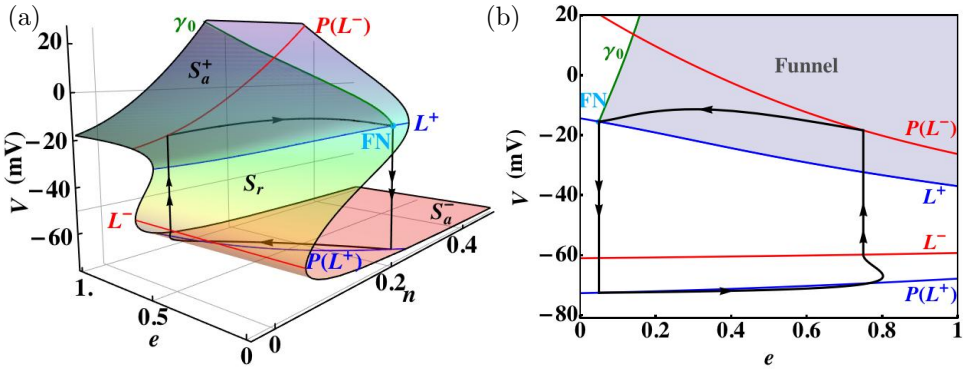


FIGURE 7. Critical manifold $S$ and singular MMO for $g_K = 4.1$ nS, $g_A = 2$ nS: (a) 3D view and (b) projection onto $(e, V)$-space. The fast jumps (double arrow) join with the slow segments (single arrow) on the attracting sheets $S_a^{\pm}$. The fold curves $L^{\pm}$ and their projections $P(L^{\pm})$ indicate where the reduced flow jumps and where it lands, respectively. The grey shaded region between $L^+$ and the strong canard (green, $\gamma_0$) is the funnel of the folded node (FN).

All other points on the folds $L^{\pm}$ are called jump points since solutions of (8) which reach $L^{\pm}$ experience a finite time blow-up and cease to exist.

3.2. **Singular periodic orbits, relaxation oscillations and MMOs.** Using the reduced and layer flows, singular periodic orbits can be constructed as continuous concatenations of reduced and layer flow trajectories (Figures 6 and 7). Singular periodic orbits which hit the upper fold curve $L^+$ at a jump point (Figure 6) correspond to relaxation oscillations [27, 34]. Singular periodic orbits which are filtered into the folded node (Figure 7) are singular representations of MMOs [2, 34].

An important diagnostic of the folded node is the eigenvalue ratio $\mu := \frac{\lambda_w}{\lambda_s}$ of the linearization of (9), where $|\lambda_w| \leq |\lambda_s|$. Using this quantity, an upper bound can be computed for the number of small oscillations seen in a MMO pattern [2, 26, 35]:

$$s \leq s_{\max} := \lfloor \frac{\mu + 1}{2\mu} \rfloor. \tag{10}$$

The distance from the phase point of global return trajectories on $P(L^-)$ to the strong canard is denoted by $\delta$ and is another important diagnostic of MMOs [2]. The convention is that a negative $\delta$ denotes orbits that land outside the funnel (Figure 6) and a positive $\delta$ denotes orbits that land inside the funnel (Figure 7). The border $\delta = 0$ marks the boundary between MMOs and relaxation oscillations and indicates that a part of the singular orbit is a segment of the strong canard.

Variation of the biophysical parameter $g_K$ affects the repolarizing current in the active phase, the dynamics of which are associated with the local oscillations in the MMOs. Consequently, $g_K$ controls (almost exclusively) the eigenvalue ratio $\mu$ of the folded node. Similarly, variation of the biophysical parameter $g_A$ affects the subthreshold current in the silent phase, the dynamics of which are associated with the global resetting properties. As a result, $g_A$ controls (almost exclusively) the distance $\delta$ of the global return trajectories from the strong canard [34]. Because of this, we use $(g_K, g_A)$ and $(\mu, \delta)$ interchangeably. Moreover, we can now justify our choice

of the special horizontal and vertical directions in Section 2. By fixing $g_A = 4$ nS and $C = 2$ pF in Section 2.1, the distance $\delta$ of the global return trajectories is also essentially fixed.[3] The only bifurcations that arise as $g_K$ varies are due to changes in the eigenvalue ratio $\mu$. By fixing $g_K = 4.1$ nS and $C = 2$ pF in Section 2.2, the eigenvalue ratio $\mu$ is fixed and the only quantity that varies is the global return of trajectories $\delta$ (through variations in $g_A$). In particular, there is a maximum number of small amplitude oscillations; for $g_K = 4.1$ nS and $C = 2$ pF resepectively $C = 0.1$ pF, we find $s_{\max} = 4$ (see Figure 3 resp. **??**), which matches our singular limit prediction, i.e. we also obtain $s_{\max} = 4$ in (10) for this specific example where $\mu \approx 0.122$.

In general, we wish to demonstrate that the singular limit systems ((4) and (5)) predict the behaviour of the full system (1) sufficiently well. Figure 5(b) shows a 2-parameter bifurcation diagram based on our singular limit analysis. The right $\mu = 1$ border of the MMO regime corresponds to a degenerate folded node where 2 nonzero eigenvalues merge. To the right of the $\mu = 1$ border we have folded foci which possess no canards and hence we predict relaxation oscillations. The left border $\mu = 0$ denotes a folded saddle node (type II) of the reduced flow [18, 26]. To the left of the $\mu = 0$ border we have a folded saddle on $L^+$ and a stable node on $S_a^+$, corresponding to a stable depolarized state of (1).

The $\delta = 0$ border indicates whether or not the global return mechanism projects the phase point of the singular orbits into the funnel. Below the $\delta = 0$ line, orbits land outside the funnel and relaxation oscillations are produced. Increasing $\delta$ to positive values moves the phase point into the funnel so that MMOs are produced. The upper boundary of the MMO regime is a curve of SNIC bifurcations. Crossing this curve towards increased $g_A$ annihilates the singular periodic orbit and a stable hyperpolarized state becomes the attractor. The predictive power of geometric singular perturbation theory for the boundaries of the MMO regime is evident from Figure 5.

3.3. **The geometry of MMOs.** We now examine the geometry of (1) away from the singular limit to explain the appearance of the small amplitude oscillations within a MMO pattern. Fenichel's invariant manifold theorems [10, 17] guarantee that the regions of $S_a^\pm, S_r$ that are $\mathcal{O}(1)$ away from $L^\pm$ perturb to invariant slow manifolds $S_{a,C}^\pm, S_{r,C}$ which are $\mathcal{O}(C)$ close to their singular counterparts. The flow on these perturbed manifolds is also a smooth $\mathcal{O}(C)$ perturbation of the flow on the critical manifold.

Extending the invariant slow manifolds by the flow of (1) into the vicinity of a folded node (where normal hyperbolicity is lost) results in a local twisting of the attracting and repelling sheets, $S_{a,C}^+$ and $S_{r,C}$, [26, 35]. This geometric feature produces the small spikes that can be seen during the active phase of the burst. Representative invariant slow manifolds calculated up to a plane $\Sigma_e : e = e_{FN}$ passing through the folded node are depicted in Figure 8. The procedure for computing $S_{a,C}^+$ and $S_{r,C}$ follows [3, 4, 5] and is outlined in Appendix A.

These rotational properties of the slow manifolds are closely related to the existence of the folded node singularity and hence to the existence of canards in (1). Away from the singular limit, a canard refers to any trajectory that passes from an attracting to a repelling slow manifold and is $\mathcal{O}(C)$ close to a repelling slow

[3] To be more precise, $\delta$ is essentially fixed if we stay away from the lower MMO boundary (period-doubling curve) in Figure 5(a).

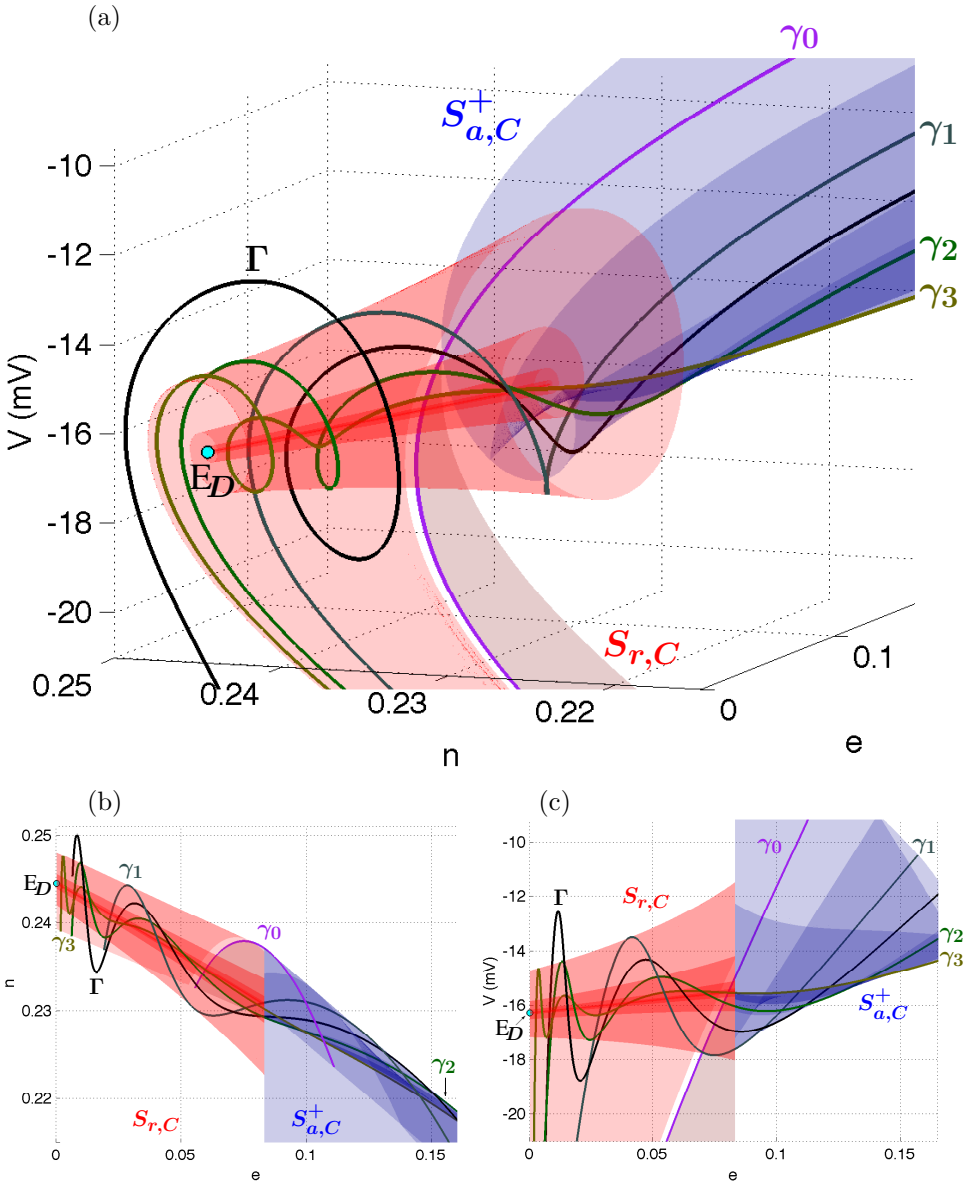


FIGURE 8. Slow manifolds $S^+_{a,C}$ and $S_{r,C}$ for $g_K = 4.1$ nS, $g_A = 1.2$ nS and $C = 2$ pF extended to cross section $\Sigma_e : e \approx 0.083$ through the folded node. The intersections are maximal canards: the primary strong canard $\gamma_0$ and the secondary canards $\gamma_l, l = 1, \ldots, 3$. Each canard is consecutively separated by a full rotation. The attractor $\Gamma$ of system (1) is a $1^2$ MMO and lies between $\gamma_1$ and $\gamma_2$ in rotational sector $I_2$. Also shown is a saddle equilibrium $E_D$ on $S_{r,C}$ (teal filled circle).

manifold for an $\mathcal{O}(1)$ time on the slow timescale. A *maximal canard* corresponds to

a transverse intersection of the slow manifolds $S^+_{a,C}$ and $S_{r,C}$ extended beyond the fold curve $L^+$. For sufficiently small perturbations $C$ (i.e. for $\varepsilon \ll 1$), there exist $s_{max}+1$ maximal canards which connect the flow from $S^+_{a,C}$ to $S_{r,C}$ and associated to each maximal canard is a whole family of canards [35].

The $1^{st}$ and $(s_{\max}+1)^{th}$ maximal canards are called the *primary strong canard* $\gamma_0$ and the *primary weak canard* $\gamma_w$, respectively. The primary strong (weak) canard corresponds to the strong (weak) eigendirection of the folded node. The remaining $s_{\max}-1$ maximal canards $\gamma_l, l = 1,\ldots,s_{\max}-1$ positioned between the primary canards are called *secondary canards*. The primary strong canard $\gamma_0$ makes one twist (half-rotation) about the primary weak canard. Each successive secondary canard $\gamma_l$ makes $l$ full rotations about the primary weak canard which serves as the axis of rotation for both the canards and invariant manifolds $S^+_{a,C}$ and $S_{r,C}$.

The funnel region between the primary canards is partitioned by the secondary canards into $s_{\max}$ subsectors $I_k, k \in [1,\ldots,s_{\max}]$ each with different rotational properties. Initial conditions in sector $I_k$ make $(2k+1)$ twists (half-rotations) about the primary weak canard. These rotations occur in a $\mathcal{O}(\sqrt{C})$ neighbourhood of the folded node. At a $\mathcal{O}(1)$ distance from the fold $L^+$, the secondary canards are $\mathcal{O}(C^{(1-\mu)/2})$ close to the strong canard whilst the width of the maximal rotation sector is $\mathcal{O}(1)$. In the singular limit, the secondary canards all collapse onto the strong canard [2, 35]. The vertical bifurcation diagrams (Figures 3 and 4) give an indication of the width of the rotational sectors $I_k$. For $g_K = 4.1$ nS, $C = 2$ pF (Figure 3), the maximal rotation sector $I_4$ is significantly larger than sectors $I_1, I_2$ and $I_3$. As $C$ decreases the secondary canards approach the strong canard and the corresponding sectors decline in width (Figure 4), except for the maximal rotation sector $I_4$ which covers (almost) the entire MMO regime.

Figure 8 shows the maximal canards which connect $S^+_{a,C}$ and $S_{r,C}$. The purple trajectory is the primary strong canard $\gamma_0$ and it makes one twist (half-rotation). The dark slate grey orbit is the first secondary canard $\gamma_1$ which makes 3 twists. The green canard is $\gamma_2$ which makes 5 twists about the axis of rotation and the olive canard $\gamma_3$ is the third secondary canard which makes 7 twists. Also shown are the saddle equilibrium $\mathrm{E}_D$ (teal point) of the system which lies on $S_{r,C}$ and the unique trajectory $\Gamma$ (black) of the system for the given parameter values corresponding to a $1^2$ MMO which lies in rotational sector $I_2$ bounded by $\gamma_1$ and $\gamma_2$.

These secondary canards explain now the boundaries shown in the interior of the MMO region in Figure 5. In the singular limit diagram, Figure 5(b), the vertical lines in the interior of the bursting region which occur at resonant values of $\mu^{-1}$ indicate candidate boundaries for the rotational sectors since a maximal canard bifurcates from the weak canard at odd integer values of $\mu^{-1}$ [35]. In order of decreasing $g_K$, the first vertical line in the interior of the MMO regime in Figure 5(b) corresponds to $\mu^{-1} = 3$. The next vertical line occurs at the $g_K$ value for which $\mu^{-1} = 5$ and so on. Clearly any bifurcation diagram we draw is incomplete, but a comparison of the singular and non-singular diagrams (Figures 5(b) and (a)) reveals a one-to-one correspondence between boundaries of the different MMO regions. Recall, all secondary canards collapse onto the strong canard ($\delta = 0$) in the singular limit. Thus the almost linear segments of the interior MMO boundaries in Figure 5(a) collapse onto the $\delta = 0$ curve in Figure 5(b) and we are left with only the vertical segments in Figure 5(b).

We turn now to more qualitative methods based on the singular perturbation analysis to further our understanding of the spike adding transitions in the MMO patterns.

4. **Return maps of MMOs.** Poincaré (first return) maps provide a tool to analyze periodic orbits and their stability [11]. In the setting of singularly perturbed problems, return maps can be used to understand the dynamics in a simple and elegant way. The essential ingredient of singularly perturbed problems that the return map formulation developed here depends upon, is the exponential contraction of the system along the attracting slow manifold $S_{a,C}$ [6, 13, 15, 19, 23, 36, 37]. Cross sections to $S_{a,C}$ quickly evolve to exponentially thin strips that can be approximated by curves. Thus, the flow map through an appropriately chosen section is strongly contracting and hence the flow map is almost 1D. Here we detail the formulation of singular and non-singular return maps which cover the essential dynamics. Our work is an amalgamation of the work done by [19, **?**, 37] and [15] who use singular and non-singular return maps, respectively. In contrast to [15, 36, 37] who use a cross-section through the folded node (i.e. use the blow-up technique), we choose a cross-section that keeps the analysis simple and retains the essential dynamics for both $\varepsilon = 0$ and $\varepsilon \neq 0$. We show that vital information can be extracted from the singular limit return map. Hence we can use the singular limit as a predictor for the non-singular case.

4.1. **Singular return maps.** Following the work of [19, 36], we first construct a singular return map to characterize the dynamics of the singular orbits [12, 16, 27]. In the singular problem (systems (4) and (5)), periodic orbits are formed from continuous concatenations of slow and fast orbit segments. For the reduced and layer flows of the lactotroph model, we define the following maps which track local and global properties of the flow:

- Trajectories of the reduced problem (4) starting from $P(L^-)$ outside the funnel can reach $L^+$ at a jump point and follow the layer flow (5) to $S_a^-$. Trajectories then follow the reduced flow on $S_a^-$ to $L^-$ where they jump and return to $P(L^-)$. This map tracks the returns of jump points (see, e.g., Figure 6) and we denote it by
$$\Pi_J : P(L^-) \to L^+ \to P(L^+) \to L^- \to P(L^-).$$
- All trajectories of the reduced problem (4) starting from $P(L^-)$ inside the funnel reach $L^+$ at the folded node point, FN $\in L^+$. Since these trajectories do not represent canards for $C \neq 0$ they jump in an $O(\sqrt{C})$ neighbourhood of the folded node point [2, 35]. This explains why we do not extend these singular canards onto $S_r$ in the singular limit but let them jump at the folded node to $S_a^-$. They then follow the reduced flow on $S_a^-$ to $L^-$ where they jump again and return to $P(L^-)$. This map tracks the returns of points in the interior of the funnel (see, e.g., Figure 7) and we denote it by
$$\Pi_F : P(L^-) \to FN \to P(L^+) \to L^- \to P(L^-).$$
- The strong canard $\gamma_0$ represents all rotational canards for $C = 0$ and hence, trajectories of (4) can track the strong canard $\gamma_0$ on $S_r$. These canard trajectories can jump off $\gamma_0$ at any point on $\gamma_0 \cap S_r$ to $S_a^-$ and flow into $L^-$ before

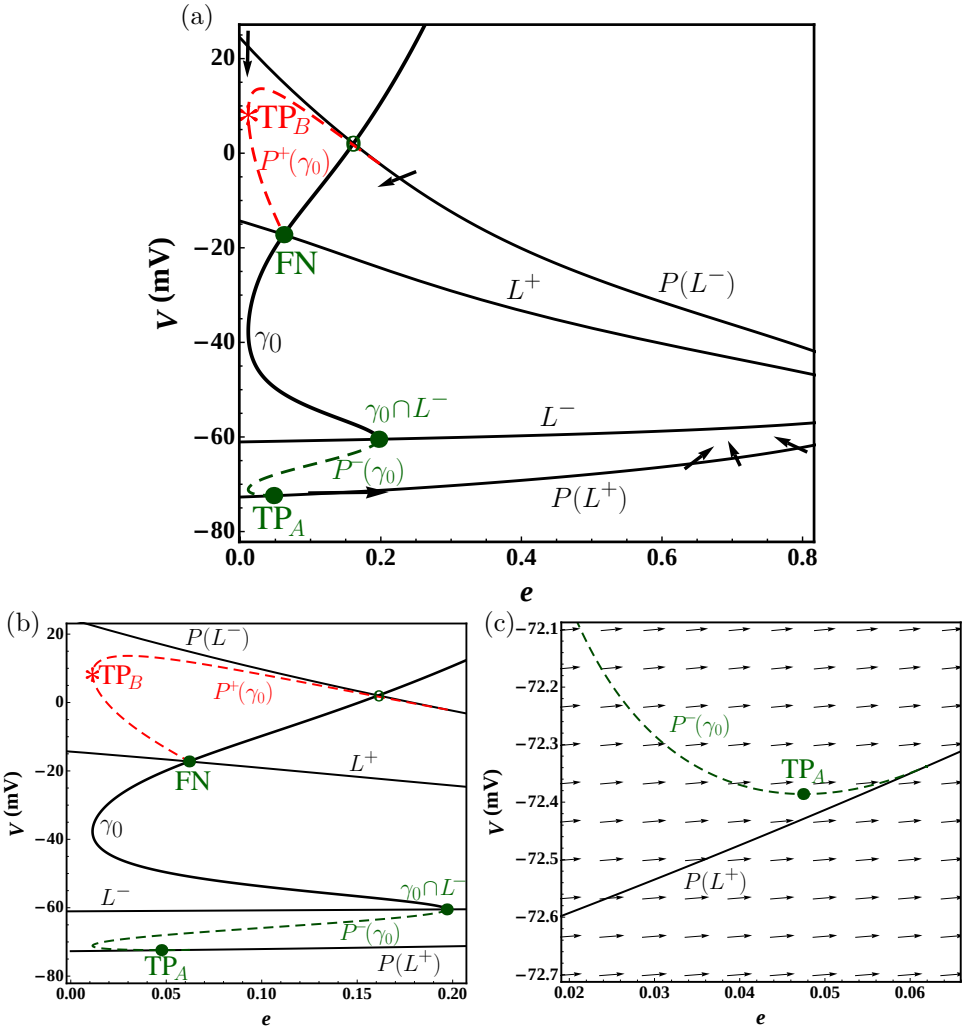


FIGURE 9. The reduced flow for $g_K = 5$ nS and $g_A = 4$ nS: panels (b) and (c) are zooms. Note that the reduced flow has a tangency with $P^+(\gamma_0)$ (red asterix TP$_B$) and $P^-(\gamma_0)$ (green circle TP$_A$, panel (c)).

jumping to $P(L^-)$. The returns of these 'jump-away' canards are monitored via this map, denoted by

$$\Pi_A : \gamma_0 \cap S_r \to S_a^- \to L^- \to P(L^-).$$

- Trajectories of (4) tracking the strong canard $\gamma_0 \cap S_r$ can also jump up to $S_a^+$, flow into $L^+$ and subsequently return to the section $P(L^-)$. This map follows the returns of the 'jump-back' canards and we denote it by

$$\Pi_B : \gamma_0 \cap S_r \to S_a^+ \to L^+ \to P(L^+) \to L^- \to P(L^-).$$

We construct the first return map $\Pi_0 : \Sigma_0 \to \Sigma_0$ as the union of the maps $\Pi_J, \Pi_F, \Pi_A$ and $\Pi_B$. We take $\Sigma_0 = P(L^-)$ as the section so that the map is

naturally parametrized by the coordinate $e$. To completely understand $\Pi_0$, the geometry of the reduced system must be examined in detail. Figure 9 shows the projection of the reduced flow (4) on the $(V, e)$ plane for the specific parameter values $g_K = 5$ nS, $g_A = 4$ nS with the strong canard $\gamma_0$ on both attracting and repelling sheets of the critical manifold. The reduced flow along $P(L^-)$ is towards $L^+$. On the other hand, the reduced flow along $P(L^+)$ is away from $L^-$ for small values of $e$ (see Figure 9(c)) and towards $L^-$ for larger values of $e$.[4]

Consider two jump points $P_1(V_1, e_1)$ and $P_2(V_2, e_2)$ on $L^+$ with $0 < e_1 < e_2 < e_{FN}$. On jumping down to $P(L^+)$ the orientation $e_1 < e_2 < e_{FN}$ is preserved. However, since the reduced flow is away from $L^-$ for small $e$ and towards $L^-$ for larger $e$, this orientation is reversed when $P_1$ and $P_2$ are flowed forward to $L^-$. That is, the $e$ coordinate of $P_2$ under the flow of (8) is to the left of the $e$ coordinate of $P_1$ under the flow of (8). Thus if we track points described by the map $\Pi_J$ then this implies a decreasing segment in the return map $\Pi_0$ due to the orientation flip caused by the reduced flow on the lower branch $S_a^-$. The corresponding (slightly) decreasing branch labelled $I_0$ is shown in Figure 10(a). Next, note that the map $\Pi_F$ maps the whole funnel segment on $P(L^-)$ to a single value. This implies a horizontal segment in the return map $\Pi_0$ which we observe as the branch $I_1$ in Figure 10(a).

The maps $\Pi_A$ and $\Pi_B$ create vertical segments in the map $\Pi_0$ due to canards [1, 37]. Thus, the singular map $\Pi_0$ is multi-valued and not well-defined. We track the first returns of $\gamma_0 \cap S_r$ to deduce the vertical extent of these segments. Both start at the point FN which is obviously the beginning of the canard segment onto $S_r$. We start with the jump-away canards. As we follow the strong canard on the repelling sheet the returns initially increase from FN until they reach the point $\mathrm{TP}_A$ (Figure 9(c)). There the projections of the jump-away canards, denoted $P^-(\gamma_0)$, have a tangency with the reduced flow. This point defines the maximum of the green vertical segment in Figure 10(a). As we follow the strong canard further on the repelling sheet the returns decrease monotonically until we reach the endpoint of $\gamma_0 \cap S_r$ at $L^-$, labelled $\gamma_0 \cap L^-$. The endpoint $\gamma_0 \cap L^-$ jumps-back to $S_a^+$, landing exactly on $P(L^-)$. The associated point on the map $\Pi_0$ is the minimum of the canard branch (Figure 10(a)). Simply put, the jump-away canards that follow $\gamma_0 \cap S_r$ the longest have the greatest vertical extent in the return map.

The projections of the jump-back canards, denoted $P^+(\gamma_0)$, also have a tangency with the reduced flow (labelled $\mathrm{TP}_B$ in Figure 9). This introduces a corresponding turning point (also labelled $\mathrm{TP}_B$ in Figure 10(a)) in the return map $\Pi_0$. We track the returns of $\gamma_0 \cap S_r$ once more, along with the return of the tangency. The jump-back canards start again at the canard point where all branches of $\Pi_0$ intersect (labelled FN in Figure 10(a)). As we travel along $\gamma_0 \cap S_r$ towards the endpoint on $L^-$, the returns increase until we encounter the tangency ($\mathrm{TP}_B$) between the projection $P^+(\gamma_0)$ and the reduced flow on $S_a^+$. This tangency corresponds to the maximum of the returns of the jump-back canards ($\mathrm{TP}_B$ in Figure 10(a)). As we trace the canard further, the returns then start to decrease from the maximum. If the projection $P^+(\gamma_0)$ lies outsi de the singular funnel, then the return of the endpoint $\gamma_0 \cap L^-$ is above the canard point of the map. On the other hand, if $P^+(\gamma_0)$ falls inside the singular funnel then the jump-back canards start at the canard point, increase to a maximum and then decrease back to the canard point. The issue is compounded by the fact that the initial point $\gamma_0 \cap P(L^-)$ which tracks

[4]This implies a point of tangency of the reduced flow with $P(L^+)$ at some $e > e_{FN}$.

the strong canard may jump off $\gamma_0 \cap S_r$ precisely to $\gamma_0 \cap P^+(\gamma_0)$, indicated with an open circle in Figure 9(a) and (b), thus generating a periodic jump-back canard cycle which cannot be detected by $\Pi_0$. This return of canards to the funnel has the potential to generate chaotic invariant sets [37]. A detailed study is left for future work.

Note that for $\mu = 1$, the strong and weak canards coincide. As $\mu$ decreases, the primary canards separate. In spite of this, neither of them connect to the saddle $\mathrm{E}_D$ on $S_r$ (not shown) and both travel along $S_r$ towards $L^-$. Consequently, the singular returns for the weak canard $\gamma_w$ are very similar to those of the strong canard $\gamma_0$. In particular, the returns of $\gamma_w$ form vertical branches in $\Pi_0$ attached to some point $e_w$ in the singular funnel. The further $\mu$ decreases from 1, the further $e_w$ moves away from FN into the funnel. Analogous to the strong canard, the endpoints of the vertical branches associated with $\gamma_w$ are the turning point corresponding to the jump-back weak canard and the termination of $\gamma_w$ on the lower fold $L^-$.

4.2. **Non-singular return maps.** For the fully perturbed problem (1) we define a similar first return map $\Pi_C : \Sigma \to \Sigma$, where $\Sigma$ is a suitably chosen cross section transverse to the flow and far from the fold and $\varepsilon = \frac{C}{k_{tg}}$. The typical choice in numerical simulations was to take the section as a line of initial conditions on the attracting slow manifold with fixed coordinate $n$:

$$\Sigma = \left\{ (V, n, e) \in S^+_{a,C} : n = n_\sigma,\ n_\sigma \text{ constant} \right\}.$$

We choose $n_\sigma$ so that we are close to the landing point of trajectories that jump up to $S^+_{a,C}$ from $S^-_{a,C}$. In most instances, we take $n_\sigma = 0.04$. As in the singular case, this choice of $\Sigma$ leads to a return map naturally parametrized by $e$. Note that such a section will cross $P(L^-)$. Thus it only covers the return map between 0 and $e_{\max}$ where $e_{\max} < 1$. Nonetheless, the essential dynamics are covered. In particular, we observe all the attractors (relaxation and mixed mode oscillators) of the system. The procedure for computing the return map $\Pi_C$ is detailed in Appendix B.

Panels (b) and (c) of Figure 10 show the map $\Pi_C$ for $C = 0.2$ pF and $C = 2$ pF, respectively. As $C$ increases, the vertical extent of the maps decreases rapidly but the structure of the singular return map $\Pi_0$ itself is preserved. The maximum associated with the turning point $\mathrm{TP}_B$ in $\Pi_0$ persists under small perturbations as a local maximum of $\Pi_C$. The fixed point (indicated by black markers) of the maps lies in rotational sector $I_1$ and the associated MMO pattern is indeed a $1^1$ MMO (Figure 10(d)).

The apparent jump in the perturbed maps is the strong canard which divides trajectories between relaxation oscillations and MMOs. These regions of rapid expansion in the maps reflect the instability of trajectories flowing along the canards on $S_{r,C}$ for various times before jumping to $S^\pm_{a,C}$ [15]. The vertical extent of these near vertical segments is not clear from the simulations due to the stiffness of the problem. To clarify, each seemingly disjoint branch of the map $\Pi_C$ is in fact continuously connected to each other. Limitations in the numerical integration scheme prevents these segments of rapid variation from being computed using initial value solvers. We use boundary value solvers instead to compute the canard segments as indicated in Appendix B.

5. **Bifurcations of the return maps.** We now use the singular and non-singular return maps $\Pi_0$ and $\Pi_C$ to track the bifurcations of MMOs in the lactotroph model (1) and show that the return maps cover the essential dynamics. Our work differs

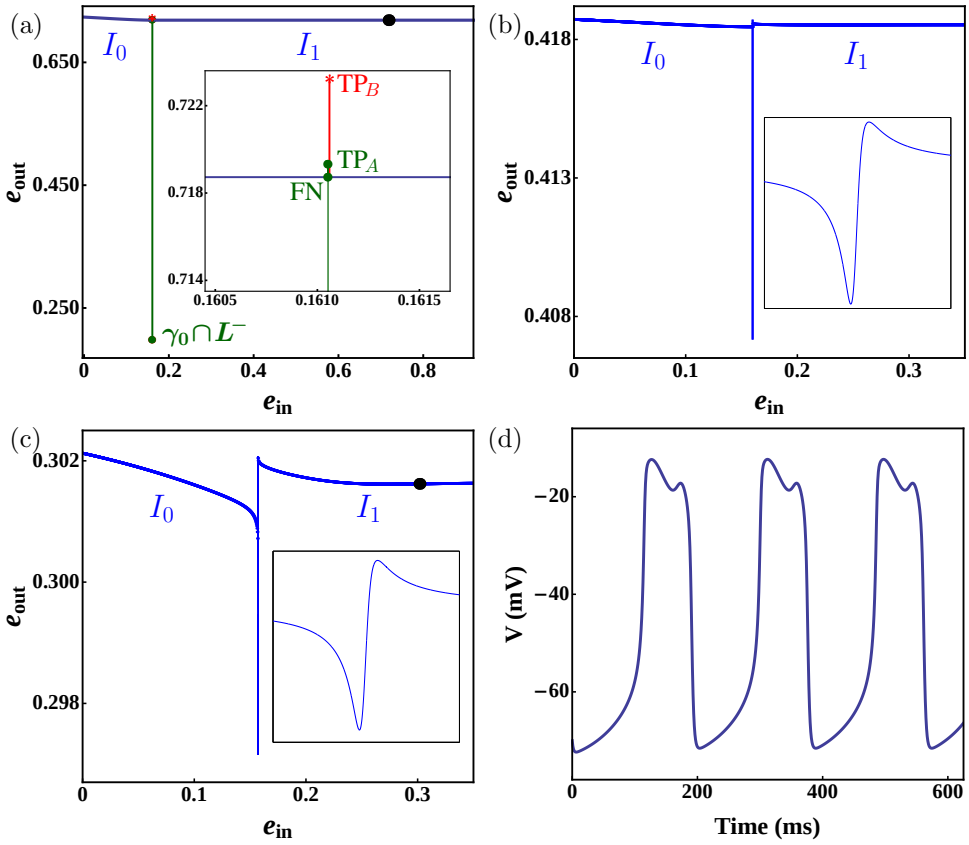


FIGURE 10. Return maps $\Pi_C$ for $g_K = 5$ nS, $g_A = 4$ nS and (a) $C = 0$ pF with inset showing the jump-back (red) and jump-away (green) canards. (b) $C = 0.2$ pF with inset showing a caricature of the vertical segment at the strong canard. (c) $C = 2$ pF. Panel (d) shows the corresponding attractor for $C = 2$ pF, a $1^1$ MMO (as predicted). Fixed points are indicated by black markers. Note in (b) the fixed point lies outside the regime covered by the map.

from [15] who employ kneading theory and numerical analysis for a qualitative and quantitative description of the bifurcation sequence related to a folded saddle node (type II). Here, we describe (qualitatively) the bifurcation sequences associated with the primary and secondary canards of a folded node. To our knowledge, there have been no prior studies of the bifurcation sequences of folded node type canards using return maps, especially near their creation (birth) at $\mu = 1$. As in Section 2, we focus on the horizontal and vertical directions in the 2-parameter diagram (Figures 2, 3 and 5). That is, we track the bifurcations which arise from variations in $\mu$ and $\delta$ via the ret urn maps.

5.1. **Horizontal bifurcations - variation of $\mu$ and birth of canards.** Fixing $g_A = 4$ nS, the distance $\delta$ from the strong canard is essentially fixed as $g_K$ varies and so the bifurcations of interest in this scenario are the ones that arise from the creation of canards.

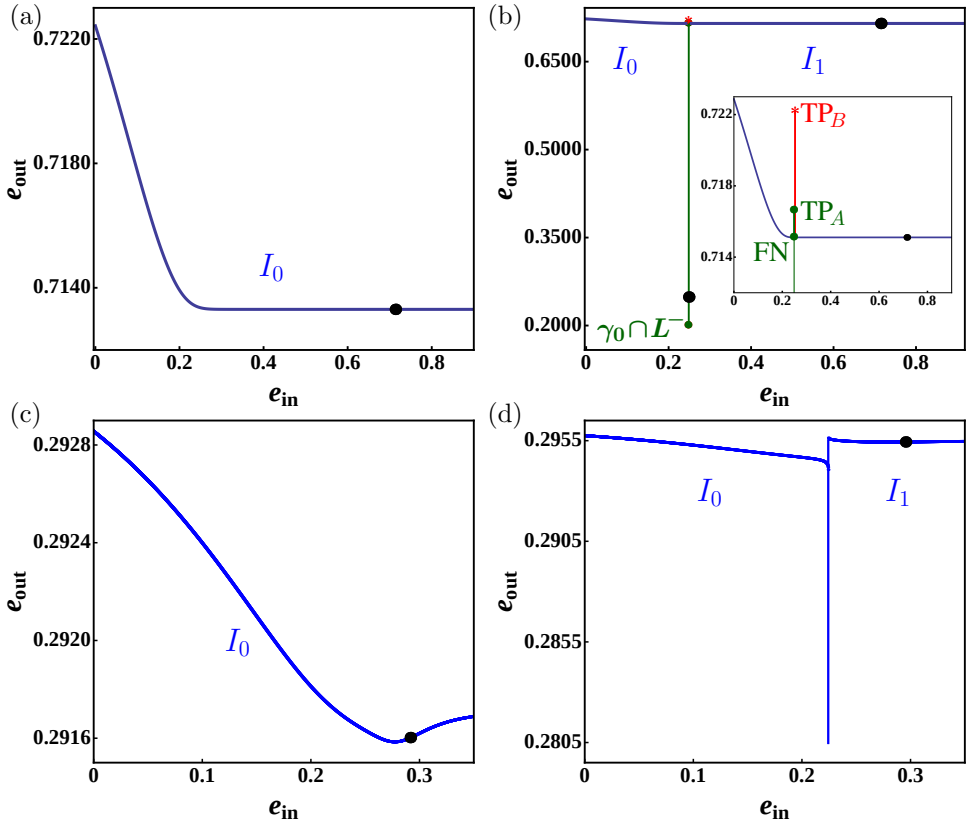


FIGURE 11. Return maps $\Pi_C$ for $g_A = 4$ nS: (a) $C = 0$ pF, $g_K = 6.2$ nS, (b) $C = 0$ pF, $g_K = 5.8$ nS, (c) $C = 2$ pF, $g_K = 6.2$ nS, (d) $C = 2$ pF, $g_K = 5.8$ nS. Fixed points are indicated by black dots.

For large $g_K$ the reduced system (4) has folded foci on $L^+$ (Figure 5), there are no canards and the singular limit map $\Pi_0$ is well defined (Figure 11(a), $g_K = 6.2$ nS). The dynamics are strongly attracting to a stable fixed point of $\Pi_0$, representing relaxation oscillations. The associated perturbed map $\Pi_C$ (Figure 11(c)) preserves this structure of $\Pi_0$. Namely, $\Pi_C$ is regular, well defined and has a single fixed point representing a relaxation oscillator.

As $g_K$ decreases so that $\mu$ becomes real, i.e. $\mu < 1$, the singular system has a folded node. There are two fixed points of the associated return map $\Pi_0$ with the stable one falling in the funnel region $I_1$ (Figure 11(b), $g_K = 5.8$ nS). For $C = 2$ pF, the corresponding $\Pi_C$ map is multimodal with two distinct branches, separated by near vertical jumps (Figure 11(d)). The left branch is the spiking branch ($I_0$). Initial conditions on this part of the map exhibit a relaxation oscillation in their transient solution. The right $I_1$ branch of the map corresponds to a $1^1$ bursting oscillation which is observed for $g_K = 5.8$ nS (Figure 2(a)) and is expected from the singular limit prediction.

To understand the whole bifurcation sequence shown in Figure 2(b), we examine the unfolding of the map as $g_K$ decreases (Figure 12). Before the degenerate folded node, the return map $\Pi_C$ is regular with a local minimum occurring in a

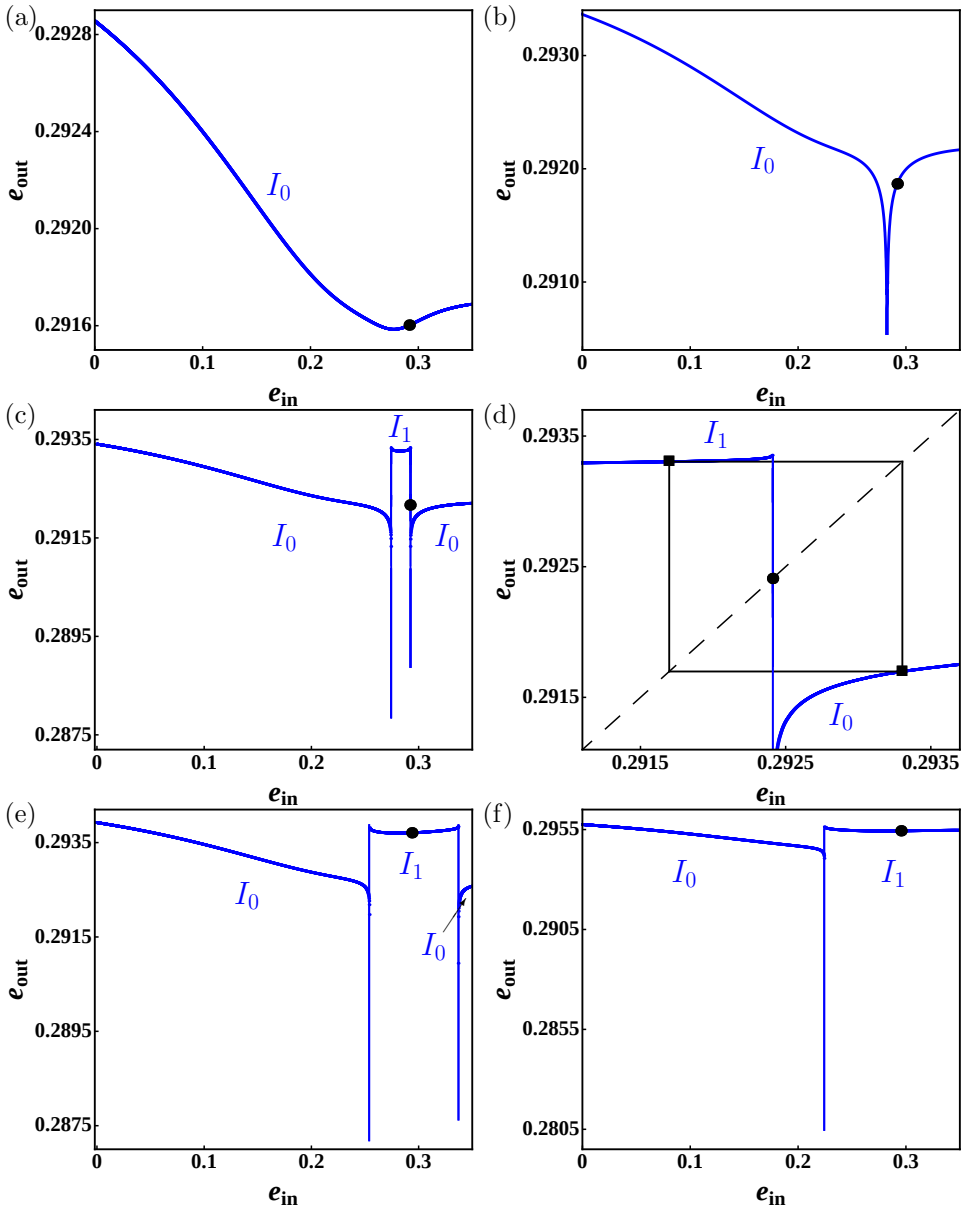


FIGURE 12. Return maps $\Pi_C$ for $C = 2$ pF and $g_A = 4$ nS: (a) $g_K = 6.2$ nS, $1^0$ spiking, (b) $g_K = 6.12824$ nS, $1^0$ spiking, (c) $g_K = 6.1225$ nS, $1^0 1^1$ MMOs, (d) Zoom of right vertical segment in (c), (e) $g_K = 6.05$ nS, $1^1$ MMOs, (f) $g_K = 5.8$ nS, $1^1$ MMOs. The strong (weak) canard corresponds to the left (right) vertical segment. Fixed points (black dots) move from $I_0$ to $I_1$. In (d), the $1^0 1^1$ MMO is represented in the maps as a 2-cycle.

neighbourhood of the folded singularity (Figure 12(a)). As $g_K$ decreases (with $\mu$

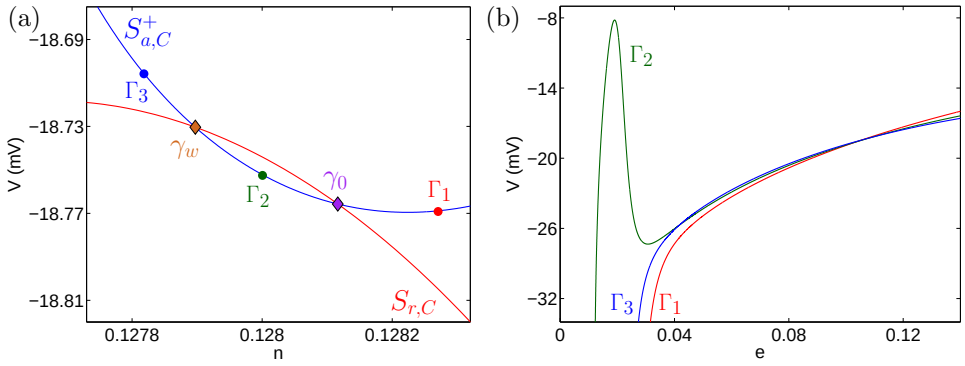


FIGURE 13. Trajectories with different rotational properties for $C = 2$ pF, $g_K = 6.1225$ nS and $g_A = 4$ nS. (a) Zoom of $S^+_{a,C} \cap \Sigma_e$ and $S_{r,C} \cap \Sigma_e$. (b) Orbit segments $\Gamma_1, \Gamma_3 \in I_0$ and $\Gamma_2 \in I_1$.

still complex), this local minimum sharpens becoming almost cusp-like and signalling the formation (bifurcation) of a canard (Figure 12(b)). When $g_K$ reaches the degenerate folded node, $\mu = 1$, the slow manifolds $S^+_{a,C}$ and $S_{r,C}$ are tangential signalling the birth of two canards, the primary strong and weak canard (left and right 'vertical branches' in Figure 12(c)-(d)) which quickly separate as $\mu$ decreases further (Figure 12(e)-(f)).

Note that just after the bifurcation the return maps have 3 distinct branches, labelled $I_0, I_1$ and $I_0$ (Figure 12(c)-(e)). The leftmost $I_0$ branch corresponds to points outside the funnel, hence the label $I_0$. The middle $I_1$ branch is the set of points in the funnel between the primary canards and the rightmost $I_0$ branch corresponds to points between the primary weak canard and the fold. Figure 13(a) shows the intersection of the slow manifolds along with the primary strong ($\gamma_0$) and weak ($\gamma_w$) canards in the cross-section $\Sigma_e : e = e_{FN}$ (see also Appendix A). We identify subsector $I_1$ as the segment of $S^+_{a,C}$ bounded by $\gamma_0$ and $\gamma_w$. The two distinct subsectors $I_0$ are then readily identified as the two disjoint parts of $S^+_{a,C}$ outside $I_1$. Also shown are 3 solutions $\Gamma_1, \Gamma_2, \Gamma_3$, taken from the sectors $I_0, I_1$ and $I_0$, respectively (Figure 13(b)). The trajectory $\Gamma_1$ starts on $S^+_{a,C}$ 'prior' to the strong canard $\gamma_0$, i.e. outside the funnel, and jumps away to more negative $V$ without making any rotations. The orbit $\Gamma_2$ however lies in the funnel region between the primary canards and makes a single rotation in its transient solution. The orbit $\Gamma_3$ starts on $S^+_{a,C}$ 'after' the weak canard and like $\Gamma_1$, has a spiking transient. As $g_K$ decreases, the $I_1$ branch quickly expands to larger $e$ values and the right $I_0$ branch is eventually pushed out of the domain covered by the map (Figure 12(f)).

The reason for the difference between $\Gamma_2$ and $\Gamma_3$ is as follows: for $1 < \mu^{-1} < 2$, $S^+_{a,C}$ makes a twist around the weak canard. Then the sector $I_1$ lies above $S_{r,C}$ after passage near the folded node (not shown) and hence jumps back to $S^+_{a,C}$ where it finishes a full rotation before jumping to $S^-_{a,C}$, which explains the rotation number $s = 1$. On the other hand, the sector $I_0$ bounded by the weak canard $\gamma_w$ and the fold $L^+$ lies after passage of the folded node below $S_{r,C}$ and hence jumps immediately to $S^-_{a,C}$ without any extra rotation which then accounts for the rotation number $s = 0$. The 2 different behaviours can be clearly observed in Figure 13(b). More generally,

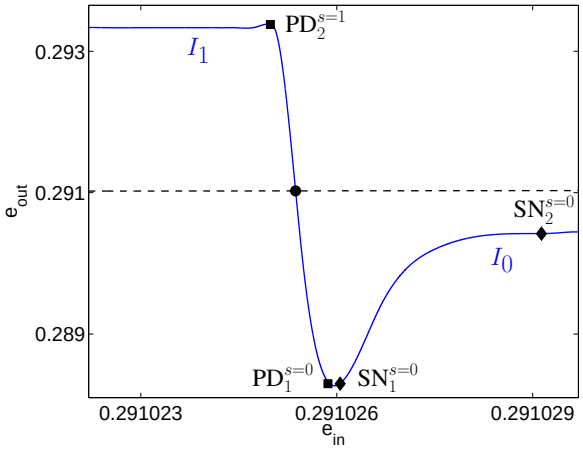


FIGURE 14. Zoom of return map $\Pi_C$ for $g_A = 4$ nS, $C = 2$ pF, $g_K = 6.1235$ nS. The fixed point (black dot) is highly unstable and the attractor is a $(1^0)^4 1^1$ MMO (not shown).

initial conditions in the region between the weak canard and the fold rotate $s_{\max} - 1$ times before jumping away to the attracting manifold (see Section 5.3).

Figure 14 shows a zoom of the return map $\Pi_C$ for $g_K = 6.1235$ nS near the vertical branch associated with the weak canard. Recall from Section 4.1 that the local maximum in Figure 14 is due to a turning point in the jump-back weak canard and the local minimum is due to the termination of the jump-away weak canard. Here, rather than consider a bifurcation diagram, we consider a single snapshot of a 3-parameter family of maps. Since the local topological structure of the map is preserved under changes in the bifurcation parameter, the only thing that changes is the position of the diagonal relative to the map. Hence we proceed on the understanding that the indicated bifurcations occur when a fixed point, i.e. an intersection of the map with the diagonal, crosses the special points. We observe that the diagonal 'moves up' relative to the map as the bifurcation parameter $g_K$ decreases. For $g_K > 6.127$ nS there is a stable fixed point to the right of the local minimum. As $g_K$ decreases the diagonal will first touch the map at the $\mathrm{SN}_1^{s=0}$ point which is followed immediately by the $\mathrm{PD}_1^{s=0}$ point where the newly created stable fixed point loses its stability. As $g_K$ decreases further, the stable spiking branch $s = 0$ loses its stability at the $\mathrm{SN}_2^{s=0}$ point. The $1^1$ MMO branch then becomes stable at $\mathrm{PD}_2^{s=1}$. In between the $\mathrm{SN}_2^{s=0}$ and the $\mathrm{PD}_2^{s=1}$ points, there is a parameter window in which there are no stable fixed points and the MMO attractor is an $n$-cycle with $k$ period-$n$ points on the $s = 0$ branch and $(n - k)$ period-$n$ points on the $s = 1$ branch where $k$ is typically either 1 or $n - 1$. The stable $1^0 1^1$ MMO pattern is identified in the map shown in Figure 12(d) as a 2-cycle. Th is explains precisely the sequence of bifurcations detected in Figure 2, which is closely related to the birth of canards.

5.2. **Vertical bifurcations - variation of $\delta$ and crossing of strong canard.** Fixing $g_K = 4.1$ nS, the maximal number of rotations is $s_{\max} = 4$. We construct the maps $\Pi_0$ and $\Pi_C$ and explore the bifurcation sequence associated with the passage

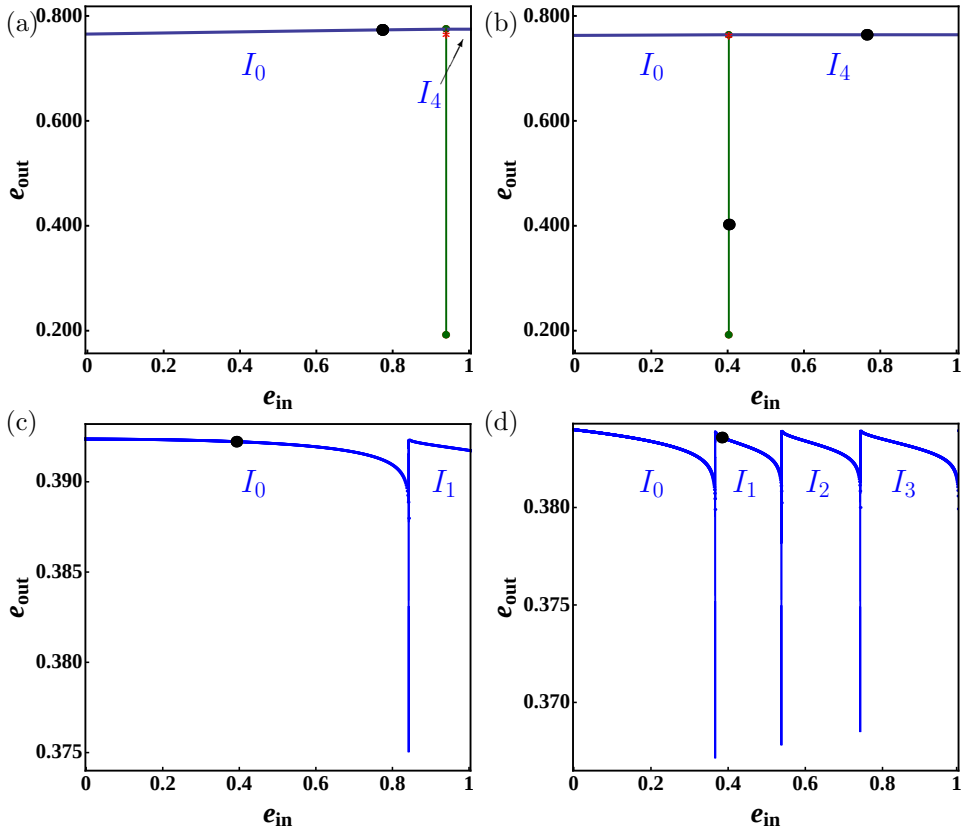


FIGURE 15. Return maps $\Pi_C$ for $g_K = 4.1$ nS where $s_{\max} = 4$: (a) $C = 0$ pF, $g_A = 0.3$ nS ($\delta < 0$), (b) $C = 0$ pF, $g_A = 0.7$ nS ($\delta > 0$), (c) $C = 2$ pF, $g_A = 0.3$ nS, (d) $C = 2$ pF, $g_A = 0.7$ nS. The fixed point (black dots) shifts from the left spiking branch to the $s = 1$ bursting branch.

of $\delta$ as it crosses zero. The return maps before and after this sequence of bifurcations are shown in Figure 15 for $C = 0$, 2 pF.

For $g_A = 0.3$ nS, the distance of the global returns from the strong canard $\delta$ is negative and the trajectories exhibit relaxation oscillations. The corresponding maps (Figure 15(a) and (c)) reflect these dynamics. The fixed point, indicated by the black dot, of the singular map $\Pi_0$ sits to the left of the canard point (Figure 15(a)). Thus the attractor is a relaxation orbit.

For $g_A = 0.7$ nS and $C = 0$ pF, the distance of the global returns $\delta$ is positive. The singular map $\Pi_0$ (Figure 15(b)) possesses two fixed points: one stable on the maximal rotation branch $I_4$ of the map and one highly unstable on the canard branch. As the perturbation $C$ is switched on, the secondary canards (which are represented in the singular limit by $\gamma_0$) bifurcate out of the strong canard. The non-singular return map $\Pi_C$ has five distinct branches with each branch separated by nearly vertical segments[5]. The leftmost branch $I_0$ corresponds to relaxation

[5]In Figure 15(d) three branches are visible, the other two exist outside the physiological domain $e > 1$

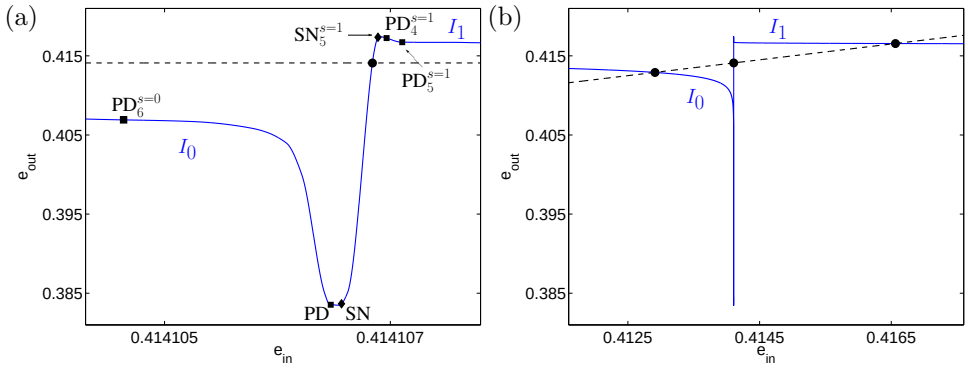


FIGURE 16. Return map $\Pi_C$ for $g_K = 4.1$ nS, $C = 2$ pF, $g_A = 0.672$ nS where $s_{\max} = 4$. The fixed point (black dots) shifts from the left spiking branch to the $s = 1$ bursting branch.

oscillations where the global return trajectories land outside the funnel (i.e. $\delta < 0$). The second branch $I_1$ of the map is the region of the funnel where MMO patterns only have one small oscillation. The subsequent branches progressively move t hrough the rotational sectors until the maximal rotation sector $I_4$ is reached. The stable fixed point of the map occurs on the $I_1$ branch and this is reflected in the observed $1^1$ MMO pattern.

When $g_A$ is small, only the spiking and first bursting branches of $\Pi_C$ lie in the physiological domain (Figure 15(c)). As $g_A$ increases, the branches of the map contract and undergo a leftward shift to smaller $e$ coordinates so that higher order bursting branches enter the physiological domain (Figure 15(d)). Consequently, the fixed point of the map occurs closer to the MMO branches of $\Pi_C$. The exact transition sequence from $I_0$ to $I_1$ can be observed in Figure 16 (which is a snapshot of $\Pi_C$ for fixed $(C, g_K, g_A)$ rather than a bifurcation diagram; compare with Figure 14). As $g_A$ continues to increase, the first intersection of the diagonal with the $s = 1$ branch occurs when $\Pi_C$ has slope 1 (bifurcation point $SN_5^{s=1}$) just before the local maximum of the jump-back canards (see also Figure 3(c)). As $g_A$ increases further, the $s = 1$ branch of the map beco mes stable as the diagonal passes through a point with slope $-1$ ($PD_4^{s=1}$) to the right of the maximum associated with the jump-back canards. Thereafter, there is a window of $g_A$ values for which there are two stable fixed points, one on the spiking branch $s = 0$ and the other on the $s = 1$ bursting branch (Figure 16(b)). There is also an highly unstable fixed point on the canard branch. As $g_A$ moves to larger values still, the fixed point on the spiking family loses stability at $PD_6^{s=0}$ point (Figure 3(c)) and the $s = 1$ MMO is the only attractor of the system. Thus the return maps $\Pi_C$ predict the sequence of bifurcations shown in Figure 3. In addition, the maps also predict the bistability of the MMO orbits.

5.3. **Crossing and creation of secondary canards.** To complete the discussion of the return maps, we examine the structure of $\Pi_C$ under two circumstances: when a trajectory crosses a secondary canard into a different rotational sector (vertical bifurcations) and when a secondary canard bifurcates from the primary weak canard (horizontal bifurcations). As seen in Section 2, the bifurcation structure of (1) follows similar trends in the transitions between MMO families under variations in $\delta$ and $\mu$. The return map $\Pi_C$ reflects this as shown in Figure 17.

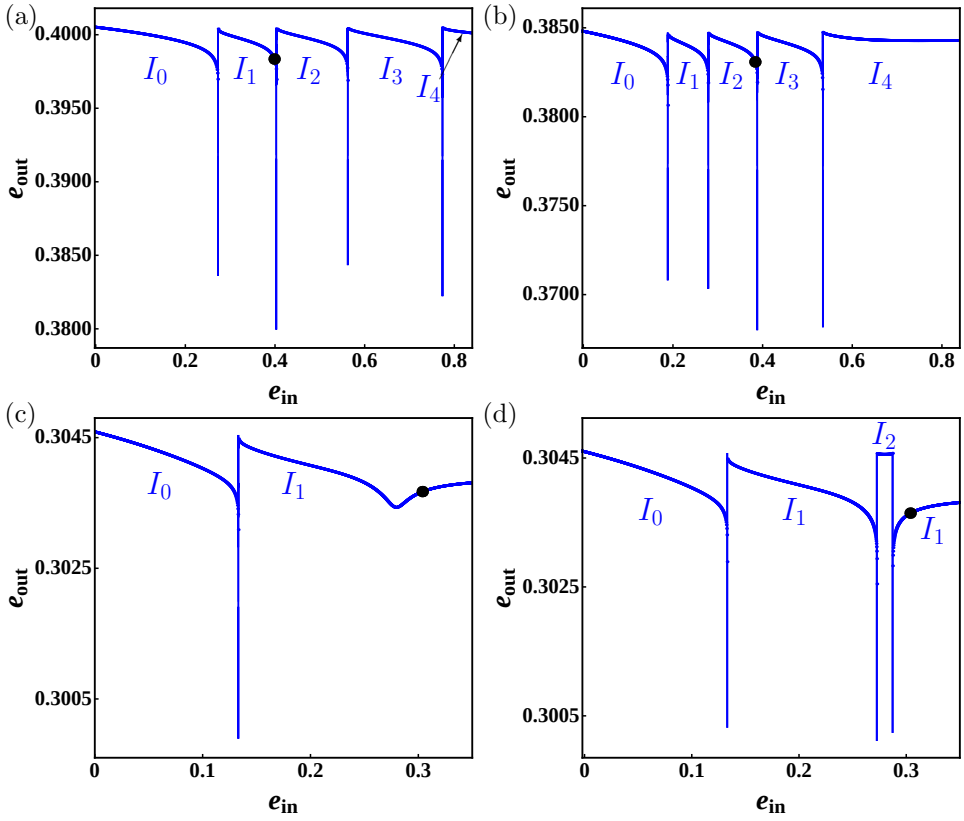


FIGURE 17. Return maps $\Pi_C$ for $C = 2$ pF under variations in $\delta$ and $\mu$: (a) $g_K = 4.1$ nS, $g_A = 1$ nS, (b) $g_K = 4.1$ nS, $g_A = 1.45$ nS, (c) $g_K = 4.723$ nS, $g_A = 4$ nS, (d) $g_K = 4.722$ nS, $g_A = 4$ nS. Black dots denote fixed points of the map.

Variations in $\delta$ have the effect of shifting the map relative to the diagonal but have virtually no impact on the structure (topology) of the map. For $g_K = 4.1$ nS, the maximal number of rotations is $s_{\max} = 4$ so the return map $\Pi_C$ has 5 branches. Starting with $g_A$ small, increasing $g_A$ shifts the diagonal to the right relative to the map so that the fixed points shift to MMO branches with higher rotation number. In terms of the funnel, orbits are pushed further and further away from the strong canard, moving deeper into the rotational subsectors. Bistable MMO orbits can also be detected near the switch from one rotational subsector to another. These manifest in the maps as two stable fixed points occurring on adjacent MMO branches.

The bifurcations that occur arise as the trajectories cross the canards. In the crossing from $s = 1$ to $s = 2$ (Figure 17(a)), the diagonal initially intersects the $s = 1$ branch at a stable fixed point. As the diagonal 'moves to the right' relative to the map (under increases in $g_A$),[6] it encounters the stable $s = 2$ branch at the $\mathrm{SN}_6^{s=2}$ point (Figure 3(c)). This stability is short-lived as the diagonal 'shifts right'

[6]Again, we think of the map frozen since its topological structure is preserved under parameter changes.

(relative to $\Pi_C$) and encounters the $\mathrm{PD}_7^{s=2}$ point where the $s = 2$ branch turns unstable. The concavity of the $s = 2$ branch allows the slope to decrease from $-1$ and then increase back to $-1$ so that the $s = 2$ MMOs regain their stability via another PD indicated by the point $\mathrm{PD}_8^{s=2}$ in Figure 3(c). As the diagonal 'shifts even further to the right' (relative to the map), the fixed po int on the $s = 1$ MMO branch passes through the PD point (labelled $\mathrm{PD}_9^{s=1}$) and becomes unstable. This is exactly the bifurcation sequence shown in Figure 3(c).

Under variations in $\mu$, secondary canards bifurcate from the weak canard thus forming new branches in the map. The creation of these new branches introduces almost vertical segments in $\Pi_C$. For $g_K = 4.723$ nS, the $1^1$ MMO is the attractor and this is represented by a stable fixed point on the $s = 1$ branch of $\Pi_C$ (Figure 17(c)). The $s = 1$ branch of the map has a local minimum, which as $g_K$ decreases, becomes significantly sharper until it reaches a SN bifurcation corresponding to $\mathrm{SN}_3^{s=2}$ in Figure 2(c). At this point the $s = 1$ branch breaks into two distinct branches with an additional, newly created $s = 2$ branch in between (Figure 17(d)). The left vertical boundary of $I_2$ corresponds to the newly created secondary canard $\gamma_1$ and it connects the left $s = 1$ branch with the newly created $s = 2$ branch. The right vertical boundary actually corresponds to the primary weak canard. Note that the rightmost $I_1$ branch is the rotational subsector bounded by the weak canard and the fold similar as in Figure 12(c) at the $\mu = 1$ bifurcation. As in the $\mu = 1$ case, the SN point corresponds to a tangency between $S_{a,C}^+$ and $S_{r,C}$ which then perturbs to transverse intersections. As $g_K$ decreases further, the $s = 2$ branch rapidly expands to larger $e$ values and the right $I_1$ branch is pushed out of the physiological domain. In this process, the right $I_1$ branch loses stability at $\mathrm{SN}_4^{s=1}$ in Figure 2(c). The $s = 2$ branch then becomes stable at $\mathrm{PD}_3^{s=2}$. The return map $\Pi_C$ and the associated bifurcation sequence (Figure 2(c)) in this case is analogous to the situation in Figure 14 (Section 5.1).

6. **Discussion.** MMOs in multiple timescale systems are the result of the combined interaction between a local mechanism and a global mechanism. The local mechanism is the folded node of the reduced flow (4) which causes a local twisting of the slow manifolds and hence local rotations of trajectories. The global mechanism is the global return which re-injects trajectories into the funnel region and thus resets the dynamics after completion of the local passage. A recent study of a pituitary lactotroph model [28, 31, 34] revealed that the bursting was the result of canard-induced MMOs. A discussion of the bifurcation structure of the MMOs was the primary focus of this paper.

We employed bifurcation analysis, geometric singular perturbation theory and return map analysis in order to examine the fine bifurcation structure of folded node type canards in (1). Each technique provided substantial information and it was their combination that allowed us to understand the phenomenon of spike-adding in pseudo-plateau bursters. We were able to determine the regions in parameter space where the spike transitions occur using a full system bifurcation analysis. We then used the singular limit as a predictor for the non-singular case. It was clear from the singular limit analysis that the appropriate parameter space to work in was $(\mu, \delta)$ space. Together, the singular and non-singular analyses allowed us to identify the origin and properties of the bursting.

To aid the analysis, we defined return maps $\Pi_0, \Pi_C$ in the singular (4), (5) and perturbed problems (1), respectively. We introduced these objects so that we could

study the dynamics of the system in the setting of 1D maps. This relied on the geometry and exponential contraction of the lactotroph model. The exponential contraction reduces the problem of studying the bifurcations of MMOs under variations of $C, \mu$ and $\delta$ to the study of bifurcations in a 3-parameter family of maps. The resulting maps $\Pi_C$ were multimodal and seemingly discontinuous. The distinct branches of the map arise from the canard orbits. Trajectories that follow a maximal canard on opposite sides of $S_{r,C}$ are torn apart and follow very different evolutions thus causing the rapid vertical expansion in the maps.

One of the strengths of the return map formulation is that the partitioning of the funnel can be characterized in a simple way. The canard trajectories act as separatrices in the return maps, clearly dividing trajectories with differing numbers of twists around the weak canard. The main insight obtained from $\Pi_0$ is the extent of the vertical segments of the canards in $\Pi_C$. Moreover, the turning points of $\Pi_0$ on $S_a^+$ have a one-to-one correspondence with local extrema in $\Pi_C$.

The main bifurcation sequences detected consist of only SN and PD points. In studying the transitions between MMO branches, this is sufficient. However as $\mu \to 0$ (FSN type II), different tools are needed to explain the bifurcation structure near the singular Hopf bifurcation [14, 18] of system (1): a task we leave to future work.

**Acknowledgments.** The authors would like to thank the referees for their helpful suggestions in giving the text focus and in streamlining the presentation. Financial support was provided by the University of Sydney to TV. TV thanks Warren Weckesser who provided meticulous support in the use of AUTO. RB was supported by NSF grant DMS 0917664.

**Appendix** A. **Computation of slow manifolds.** We refer to [3, 4, 5], whose work we reproduce in the context of (1), for details of the computation of the slow manifolds. To compute the slow manifolds in the case of a folded node, we consider a rescaled version of (1)

$$(\dot{V}, \dot{n}, \dot{e}) = T((C/k_t g_{\max})^{-1} f, g_1, g_2), \tag{11}$$

where the free parameter $T$ is the actual integration time. Thus the integration time of any solution is rescaled to 1. For the computation of the slow attracting manifold $S_{a,C}^+$, we continue solutions of (11) subject to boundary conditions which ensure that solutions lie (approximately) on $S_{a,C}^+$. To do this, we choose a curve on the attracting sheet of the critical manifold $S_a^+$ that is sufficiently far from $L^+$:

$$\mathbf{u}(0) \in \{(V, n, e) \in S_a : e = 0.6\}, \tag{12}$$

where $\mathbf{u} = (V, n, e)$. To ensure the relevant part of $S_{a,C}^+$ is computed near the folded node, the right endpoint $\mathbf{u}(1)$ is restricted to a plane through the folded node with the requirement that the plane is transverse to the flow. A suitable choice is to take the plane of constant $e$ passing through the folded node

$$\mathbf{u}(1) \in \Sigma_e \equiv \{(V, n, e) : e = e_{FN}\}. \tag{13}$$

Before $S_{a,C}^+$ can be calculated, note that a solution of the boundary value problem (BVP) (11) subject to (12) and (13) is the trivial orbit segment given by the folded node. We now use an homotopy method to construct a first solution of the BVP.

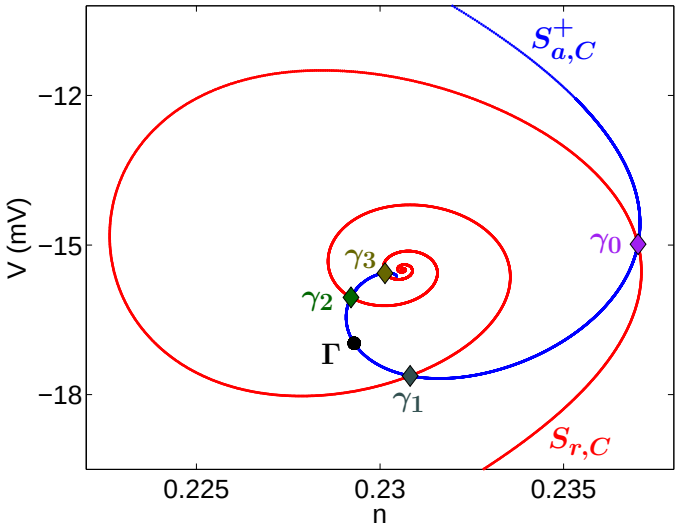


FIGURE 18. Slow manifolds $S^+_{a,C} \cap \Sigma_e$ and $S_{r,C} \cap \Sigma_e$ for $C = 2$ pF, $g_K = 4.1$ nS, $g_A = 1.2$ nS shown in cross-section $\Sigma_e : e = e_{FN}$. The intersections are maximal canards as shown in Figure 8. The outermost intersection is the primary strong canard $\gamma_0$. Subsequent intersections are the secondary canards $\gamma_l, l = 1, 2, 3$. The black dot is the intersection of the periodic orbit $\Gamma$ of the system, a $1^2$ MMO.

Starting with the trivial solution at the folded node, we continue the orbit in $T$ subject to the modified boundary condition

$$\mathbf{u}(0) \in \left\{(V, n, e) \in L^+\right\}$$

until the endpoint $\mathbf{u}(0)$ is at some predetermined distance from the folded node. In our computations, the calculation was terminated when the endpoint reached $e = 0.6$. The last solution obtained from the homotopy is the start solution for the BVP defined by (11) together with (12), (13). Numerical continuation in $T$ then generates the surface $S^+_{a,C}$.

The repelling slow manifold is computed in a similar way but with negative $T$ which has the effect of reversing the direction of the flow. The boundary conditions are chosen to ensure that solutions lie close to $S_{r,C}$. To continue orbits with negative $T$ in practice, we simply swap the boundary conditions. Thus, the BVP for the repelling slow manifold is (11) subject to

$$\begin{aligned} &\mathbf{u}(0) \in \Sigma_e, \\ &\mathbf{u}(1) \in \{(V, n, e) \in S_r : V = -30\}. \end{aligned} \tag{14}$$

As in the computation for $S^+_{a,C}$, the trivial orbit segment at the folded node is used as a starting solution for a 2-step homotopy process to find a first solution to the BVP defined by (11) subject to (14). In the first stage of the 2-step homotopy, we move solutions along $L^+$ until $e(1) = 0.01$. From there, the second stage of the homotopy moves solutions along $S_r$ until $V = -30$.

The advantage of terminating the computation of $S^+_{a,C}$ and $S_{r,C}$ at the plane $\Sigma_e$ is that canard solutions are easily identifiable as transverse intersections of the slow

manifolds (Figure 18). In terms of the BVP, canards are solutions of (11) subject to the boundary conditions

$$\mathbf{u}(0) \in \left\{(V,n,e) \in S_a^+ : V = 100\right\} \text{ and } \mathbf{u}(1) \in \{(V,n,e) \in S_r : V = -30\}.$$

A solution of this BVP is computed by finding orbit segments $\mathbf{u}_a \in S_{a,C}^+$ and $\mathbf{u}_r \in S_{r,C}$ that match in the plane $\Sigma_e$. We concatenate $\mathbf{u}_a$ with the reverse of $\mathbf{u}_r$ (so that the integration time is positive), rescale the resulting orbit back to the time interval $[0,1]$ and continue the solution. Provided $|\mathbf{u}_a(0) - \mathbf{u}_r(0)|$ is sufficiently small, a Newton step in AUTO generates a solution of the BVP which represents the respective canard solution.

**Appendix** B. **Computation of non-singular return maps.** As in Appendix A we consider (1) in its rescaled form (11). Computation of the non-singular return map $\Pi_C$ involves 2 parts: computing the regular parts of $\Pi_C$ away from the canards and approximating the exponentially thin (or nearly vertical) segments near a canard.

For the parts of $\Pi_C$ away from the canards, we require a set of initial conditions on the attracting slow manifold $S_{a,C}^+$ with $n = n_\sigma$. To initialize the computation of $\Pi_C$, we first take a line of initial conditions on the attracting sheet of the critical manifold $S_a^+$ far from the section $\Sigma$ of interest:

$$\mathbf{u}(0) \in \left\{(V,n,e) \in S_a^+ : V = 100\right\}. \tag{15}$$

This line of initial conditions is then flowed forward until they hit the section $\Sigma$, at which point the calculation is terminated. That is,

$$\mathbf{u}(1) \in \Sigma \equiv \{(V,n,e) : n = n_\sigma,\ n_\sigma \text{ constant}\}. \tag{16}$$

Exponential contraction of system (1) ensures that this curve is sufficiently close to $S_{a,C}^+$. We use this curve $S_{a,C}^+ \cap \Sigma$ as the initial conditions in our return map $\Pi_C$ and flow them forward until they return to $\Sigma$. This produces a return map naturally parametrized by the coordinate $e$. For any maximal canards that are crossed, there is a seemingly discontinuous jump and the map appears to have disjoint branches. The distance $\Delta e$ between the distinct branches (where there is no data) is nonzero and depends on the number of points used to compute $\Pi_C$. The more points used to parametrize $S_{a,C}^+ \cap \Sigma$, the smaller the 'gap' $\Delta e$. In our calculations, we typically used 2000 points.

By continuity of solutions of (1), all branches of the map are in fact continuously connected to each other by exponentially thin canard segments. To compute these canard segments, we first use AUTO to identify the maximal canards (see Appendix A). The endpoint of the canard on $S_r$ is then extended as close to the lower fold curve $L^-$ as possible to give an indication of the vertical extent of the canards. We also extend the endpoint of the canards on $S_a$ out to the section $\Sigma_V : V = 100$ and then flow it forward to obtain the corresponding canard point on $S_{a,C}^+ \cap \Sigma$. The canard point in $S_{a,C}^+ \cap \Sigma$ always sits in the interval of width $\Delta e$ between the distinct branches of $\Pi_C$.

We then take the points of the canard on $S_{r,C}$ and perturb them in either $V$ direction (towards either $S_{a,C}^\pm$). Those points that sit above the repelling slow manifold jump-back to $S_{a,C}^+$ whilst those that sit below $S_{r,C}$ jump-away to $S_{a,C}^-$. The returns of these points to the section $\Sigma$ give the returns of the jump-back and jump-away canards. To complete the computation of the return map, we must

determine the initial conditions in $\Sigma$ corresponding to the jump-back and jump-away canards. Since it is impossible to trace the returns of these canards to their origin in the section $\Sigma$, we use interpolation to approximate the distribution of these returns in a neighbourhood of the canard point. As in [15] we terminate the canard branch when it intersects the regular part of $\Pi_C$ so that we have a continuous map.

## REFERENCES


[1] K. Bold, C. Edwards, J. Guckenheimer, S. Guharay, K. Hoffman, J. Hubbard, R. Oliva and W. Weckesser, *The forced van der Pol equation. II. Canards in the reduced system*, SIAM Journal of Applied Dynamical Systems, **2** (2003), 570–608.

[2] M. Brøns, M. Krupa and M. Wechselberger, *Mixed mode oscillations due to the generalized canard phenomenon*, in "Bifurcation Theory and Spatio-Temporal Pattern Formation," Fields Institute Communications, **49**, Amer. Math. Soc., Providence, RI, (2006), 39–63.

[3] M. Desroches, B. Krauskopf and H. M. Osinga, *The geometry of slow manifolds near a folded node*, SIAM Journal of Applied Dynamical Systems, **7** (2008), 1131–1162.

[4] M. Desroches, B. Krauskopf and H. M. Osinga, *Mixed-mode oscillations and slow manifolds in the self-coupled Fitzhugh-Nagumo system*, Chaos, **18** (2008), 015107, 8 pp.

[5] M. Desroches, B. Krauskopf and H. M. Osinga, *Numerical continuation of canard orbits in slow-fast dynamical systems*, Nonlinearity, **23** (2010), 739–765.

[6] M. Desroches, J. Guckenheimer, B. Krauskopf, C. Kuehn, H. M. Osinga and M. Wechselberger, *Mixed-mode oscillations with multiple time scales*, SIAM Review, to appear.

[7] E. J. Doedel, *AUTO: A program for the automatic bifurcation analysis of autonomous systems*, Congr. Numer., **30** (1981), 265–284.

[8] E. J. Doedel, A. R. Champneys, T. F. Fairgrieve, Y. A. Kuznetsov, K. E. Oldeman, R. C. Paffenroth, B. Sandstede, X. J. Wang and C. Zhang, *AUTO-07P: Continuation and bifurcation software for ordinary differential equations*. Available from: `http://cmvl.cs.concordia.ca/`.

[9] I. Erchova and D. J. McGonigle, *Rhythms of the brain: An examination of mixed mode oscillation approaches to the analysis of neurophysiological data*, Chaos, **18** (2008), 015115, 14 pp.

[10] N. Fenichel, *Geometric singular perturbation theory for ordinary differential equations*, Journal of Differential Equations, **31** (1979), 53–98.

[11] J. Guckenheimer and P. Holmes, "Nonlinear Oscillations, Dynamical Systems, and Bifurcations of Vector Fields," Springer, 1983.

[12] J. Guckenheimer, M. Wechselberger and L.-S. Young, *Chaotic attractors of relaxation oscillations*, Nonlinearity, **19** (2006), 701–720.

[13] J. Guckenheimer, *Return maps of folded nodes and folded saddle-nodes*, Chaos, **18** (2008), 015108, 9 pp.

[14] J. Guckenheimer, *Singular Hopf bifurcation in systems with two slow variables*, SIAM Journal of Applied Dynamical Systems, **7** (2008), 1355–1377.

[15] J. Guckenheimer and C. Scheper, *A geometric model for mixed-mode oscillations in a chemical system*, SIAM Journal of Applied Dynamical Systems, **10** (2011), 92–128.

[16] R. Haiduc, *Horseshoes in the forced van der Pol system*, Nonlinearity, **22** (2009), 213–237.

[17] C. K. R. T. Jones, *Geometric singular perturbation theory*, in "Dynamical Systems" (ed. R. Johnson), Lecture Notes in Mathematics, Springer, New York, (1995), 44–120.

[18] M. Krupa and M. Wechselberger, *Local analysis near a folded saddle-node singularity*, Journal of Differential Equations, **248** (2010), 2841–2888.

[19] C. Kuehn, *On decomposing mixed-mode oscillations and their return maps*, Chaos, **21** (2011) 033107, 15 pp.

[20] Y. A. Kuznetsov, "Elements of Applied Bifurcation Theory," $3^{rd}$ edition, Springer-Verlag, New York, 2004.

[21] A. P. LeBeau, A. B. Robson, A. E. McKinnon and J. Sneyd, *Analysis of a reduced model of corticotroph action potentials*, Journal of Theoretical Biology, **192** (1998), 319–339.

[22] J. E. Lisman, *Bursts as a unit of neural information: Making unreliable synapses reliable*, Trends in Neuroscience, **20** (1997), 38–43.

[23] A. Milik, P. Szmolyan, H. Loeffelmann and E. Groeller, *Geometry of mixed-mode oscillations in the 3-d autocatalator*, International Journal of Bifurcation and Chaos, **8** (1998), 505–519.

[24] H. M. Osinga and K. Tsaneva-Atanasova, *Dynamics of plateau bursting depending on the location of its equilibrium*, Journal of Neuroendocrinology, **22** (2010), 1301–1314.
[25] S. S. Stojilkovic, H. Zemkova and F. Van Goor, *Biophysical basis of pituitary cell type-specific $Ca^{2+}$ signaling-secretion coupling*, Trends in Endocrinology and Metabolism, **16** (2005), 152–159.
[26] P. Szmolyan and M. Wechselberger, *Canards in $\mathbb{R}^3$*, Journal of Differential Equations, **177** (2001), 419–453.
[27] P. Szmolyan and M. Wechselberger, *Relaxation oscillations in $\mathbb{R}^3$*, Journal of Differential Equations, **200** (2004), 69–104.
[28] J. Tabak, N. Toporikova, M. E. Freeman and R. Bertram, *Low dose of dopamine may stimulate prolactin secretion by increasing fast potassium currents*, Journal of Computational Neuroscience, **22** (2007), 211–222.
[29] W. Teka, K. Tsaneva-Atanasova, R. Bertram and J. Tabak, *From plateau to pseudo-plateau bursting: Making the transition*, Bulletin of Mathematical Biology, **73** (2011), 1292–1311.
[30] D. Terman, *Chaotic spikes arising from a model of bursting in excitable membranes*, SIAM Journal of Applied Mathematics, **51** (1991), 1418–1450.
[31] N. Toporikova, J. Tabak, M. E. Freeman and R. Bertram, *A-type $K^+$ current can act as a trigger for bursting in the absence of a slow variable*, Neural Computation, **20** (2008), 436–451.
[32] K. Tsaneva-Atanasova, A. Sherman, F. Van Goor and S. S. Stojilkovic, *Mechanism of spontaneous and receptor-controlled electrical activity in pituitary somatotrophs: Experiments and theory*, Journal of Neurophysiology, **98** (2007), 131–144.
[33] K. Tsaneva-Atanasova, H. M. Osinga, T. Rieb and A. Sherman, *Full system bifurcation analysis of endocrine bursting models*, Journal of Theoretical Biology, **264** (2010), 1133–1146.
[34] T. Vo, R. Bertram, J. Tabak and M. Wechselberger, *Mixed mode oscillations as a mechanism for pseudo-plateau bursting*, Journal of Computational Neuroscience, **28** (2010), 443–458.
[35] M. Wechselberger, *Existence and bifurcation of canards in $\mathbb{R}^3$ in the case of a folded node*, SIAM Journal of Applied Dynamical Systems, **4** (2005), 101–139.
[36] M. Wechselberger and W. Weckesser, *Bifurcations of mixed-mode oscillations in a stellate cell model*, Physica D, **238** (2009), 1598–1614.
[37] M. Wechselberger and W. Weckesser, *Homoclinic clusters and chaos associated with a folded node in a stellate cell model*, DCDS-S, **2** (2009), 829–850.
[38] M. Wechselberger, *Á propos de canards (Apropos canards)*, Transactions of the American Mathematical Society, **364** (2012), 3289–3309.
[39] M. Zhang, P. Goforth, R. Bertram, A. Sherman and L. Satin, *The $Ca^{2+}$ dynamics of isolated mouse $\beta$-cells and islets: Implications for mathematical models*, Biophysical Journal, **84** (2003), 2852–2870.

Received June 2011 for publication.

*E-mail address*: theodore.vo@sydney.edu.au
*E-mail address*: bertram@math.fsu.edu
*E-mail address*: martin.wechselberger@sydney.edu.au